



**HAL**  
open science

# Chemo-kinematics of the Milky Way spiral arms and bar resonances: Connection to ridges and moving groups in the solar vicinity

Sergey Khoperskov, Ortwin Gerhard

## ► To cite this version:

Sergey Khoperskov, Ortwin Gerhard. Chemo-kinematics of the Milky Way spiral arms and bar resonances: Connection to ridges and moving groups in the solar vicinity. *Astronomy and Astrophysics - A&A*, 2022, 663, 10.1051/0004-6361/202141836 . insu-03849382

**HAL Id: insu-03849382**

**<https://insu.hal.science/insu-03849382>**

Submitted on 11 Nov 2022

**HAL** is a multi-disciplinary open access archive for the deposit and dissemination of scientific research documents, whether they are published or not. The documents may come from teaching and research institutions in France or abroad, or from public or private research centers.

L'archive ouverte pluridisciplinaire **HAL**, est destinée au dépôt et à la diffusion de documents scientifiques de niveau recherche, publiés ou non, émanant des établissements d'enseignement et de recherche français ou étrangers, des laboratoires publics ou privés.

# Chemo-kinematics of the Milky Way spiral arms and bar resonances: Connection to ridges and moving groups in the solar vicinity

Sergey Khoperskov<sup>1,2,3,4</sup> and Ortwin Gerhard<sup>2</sup>

<sup>1</sup> Leibniz-Institut für Astrophysik Potsdam (AIP), An der Sternwarte 16, 14482 Potsdam, Germany

e-mail: [sergey.khoperskov@gmail.com](mailto:sergey.khoperskov@gmail.com)

<sup>2</sup> Max-Planck-Institut für extraterrestrische Physik, Gießenbachstrasse 1, 85748 Garching, Germany

<sup>3</sup> Institute of Astronomy, Russian Academy of Sciences, 48 Pyatnitskaya St., Moscow, 119017, Russia

<sup>4</sup> GEPI, Observatoire de Paris, Université PSL, CNRS, 5 Place Jules Janssen, 92190 Meudon, France

Received 21 July 2021 / Accepted 25 November 2021

## ABSTRACT

Making use of a new high-resolution spiral galaxy simulation as well as *Gaia* DR2 and EDR3 data complemented by chemical abundances from the Galah DR3, APOGEE DR16, and LAMOST DR5 surveys, we explore the possible link between the Milky Way (MW) spiral arms,  $(R, v_\phi)$  ridges, and moving groups in local  $v_R$ - $v_\phi$  space. We show that the tightly wound main spiral arms in the  $N$ -body simulation can be successfully identified using overdensities in angular momentum (AM) or guiding space and also in the distribution of dynamically cold stars close to their guiding centres. Stars in the AM overdensities that travel over many kiloparsec in radius trace extended density ridges in  $(R, v_\phi)$  space and overdensities in the  $v_R$ - $v_\phi$  plane of a solar neighbourhood (SNd)-like region, similar to those observed in the *Gaia* data. Similarly, the AM space of the MW contains several overdensities that correlate with a wave-like radial velocity pattern; this pattern is also reproduced by stars well beyond the SNd. We find that the fraction of *Gaia* stars located near their guiding centres shows three large-scale structures that approximately coincide with the MW spiral arms traced by distributions of maser sources in the Sagittarius, Local, and Perseus arms. This approach does not work for the Scutum arm near the end of the bar. Similar to the simulation, the stars in the AM overdensities follow the main  $(R, v_\phi)$  density ridges with nearly constant angular momentum. When these ridges cross the SNd, they can be matched with the main  $v_R$ - $v_\phi$  features. Thus we suggest that the Hat is the inner tail of the Perseus arm, one of the Hercules components is the Sagittarius arm, and the Arcturus stream is likely to be the outermost tail of the Scutum-Centaurus arm. Based on previous work, the bar corotation is suggested to coincide with the second,  $v_\phi \approx -55 \text{ km s}^{-1}$  Hercules stream ridge, and the OLR with the Sirius stream. The latter is supported by a sharp decrease in mean metallicity beyond the Sirius stream, which is an expected behaviour of the OLR, limiting migration of the metal-rich stars from the inner MW. In various phase-space coordinates, the AM overdensity stars have a mean metallicity that is systematically higher by about 0.05 dex than the metallicity of the surrounding stars. This is a predicted behaviour of the spiral arms. We show that the wave-like metallicity pattern can be traced at least up to  $|z| \approx 1 \text{ kpc}$ . It is linked to radial velocity variations seen even farther ( $|z| \approx 2 \text{ kpc}$ ) from the Galactic mid-plane.

**Key words.** Galaxy: kinematics and dynamics – Galaxy: structure – Galaxy: abundances – galaxies: evolution – galaxies: kinematics and dynamics – galaxies: structure

## 1. Introduction

The Milky Way (MW) disk has a complex kinematic structure (see e.g. Siebert et al. 2011; Williams et al. 2013) that is likely affected by the central bar and the Galactic spiral arms (Siebert et al. 2012; Grand et al. 2015). Moreover, the Galactic disk is also perturbed externally by its satellites, in particular, by the Sagittarius dwarf galaxy (see e.g. Purcell et al. 2011; Gómez et al. 2013). The non-axisymmetric density structures in the disk and external interactions leave signatures in the kinematics of the MW stars, consistent with the presence of multiple substructures in the solar neighbourhood (SNd) (e.g., Dehnen 1998; Arifyanto & Fuchs 2006; Famaey et al. 2008; Antoja et al. 2008).

The recent data releases DR2 and EDR3 of ESA's *Gaia* mission (Gaia Collaboration 2018a, 2021a) have made it possible to deepen our understanding of the known velocity and phase-space features, and also enabled discovering many new ones. In the extended SNd, the *Gaia* data have provided more evidence

for the lack of equilibrium of the MW disk. For instance, previously known vertical wave-like motions (Widrow et al. 2012) were detected in  $z - v_z$  space in the form of a snail-like structure (Antoja et al. 2018). The precise measurements from *Gaia* also provided a more comprehensive view on the in-plane phase-space structure of the MW (Gaia Collaboration 2018a; Kawata et al. 2018; Antoja et al. 2018), allowing a number of radially extended features and short kinematic arches to be identified in  $v_R$ - $v_\phi$  velocity space (Ramos et al. 2018; Khanna et al. 2019; Kushniruk & Bensby 2019). These complex stellar motions are not easily interpreted by a single mechanism. However, several attempts have been made to explain the origin of various features, involving spiral arms (Sellwood et al. 2019; Hunt et al. 2018, 2019; Barros et al. 2020), bar resonances (Fragkoudi et al. 2019; Monari et al. 2019a,b) and external intruders (Laporte et al. 2019; Bland-Hawthorn & Tepper-García 2021).

Over the decades, much attention was paid to the agglomeration of stars in  $v_R$ - $v_\phi$  kinematic space called the Hercules stream (or the  $u$ -anomaly), with an asymmetric drift of about

$-45 \text{ km s}^{-1}$  and negative radial velocity. After *Gaia* DR2, it became clear that the Hercules stream consists of at least two elongated features (Gaia Collaboration 2018a). For a long time, numerical works and analytic calculations had argued that this stream can be explained as the effect of the MW bar if the Sun is placed just outside its outer Lindblad resonance (OLR). Then Hercules arises naturally from resonant interaction between the disk stars and a short ( $\approx 3$  kpc), fast-rotating bar (Dehnen 2000; Fux 2001; Antoja et al. 2009, 2014; Monari et al. 2017). The alternative idea, supported by more recent work on the structure and dynamics of the bulge and bar (Wegg et al. 2015; Portail et al. 2017) as well as by subsequent chemo-kinematical measurements (Bovy et al. 2019; Wegg et al. 2019), suggests that the Hercules stream is related to the corotation resonance (Pérez-Villegas et al. 2017a; Monari et al. 2019b; Binney 2020), which requires a slowly rotating long bar ( $\approx 4.5$  kpc, see e.g. Clarke et al. 2019; Sanders et al. 2019; Bovy et al. 2019).

The spiral structure is also believed to perturb the kinematics in the SNd, creating multiple overdensities in  $v_R$ - $v_\phi$  space (Quillen et al. 2011; Antoja et al. 2011; Monari et al. 2016a). Quillen et al. (2018) suggested that the ridges and arcs seen in the local velocity distributions are consistent with the presence of multiple spiral arms (see also Hunt et al. 2018; Michtchenko et al. 2018; Barros et al. 2020), which may be transient structures (Hunt et al. 2019). The properties of the MW spiral structure are less constrained than those of the Galactic bar because most of our knowledge about the spiral arms is based on HII regions (Georgelin & Georgelin 1976; Russeil 2003), giant molecular clouds (see e.g. Cohen et al. 1986; Dame et al. 1986; Grabelsky et al. 1988; Hou et al. 2009), pulsar dispersion measures (see e.g. Taylor & Cordes 1993), the distribution of young star-forming regions (see e.g. Hou & Han 2014; Reid et al. 2014, 2019), and the analysis of extinction maps (see e.g. Marshall et al. 2006; Lallement et al. 2019; Hottier et al. 2020). Then the number of arms and their precise locations and strength can only be constrained indirectly by modelling the phase-space features in the disk (see e.g. Siebert et al. 2012; Grand et al. 2015).

Interactions with satellites often trigger the formation of spiral arms (see e.g. Quinn & Goodman 1986; Dobbs et al. 2010; Pettitt & Wadsley 2018) and could perhaps even stimulate the formation of bars (see e.g. Gerin et al. 1990; Mayer & Wadsley 2004). Therefore, it is natural to assume that the external perturbations affect the kinematics of the disk, including the local SNd kinematics (see e.g. Minchev et al. 2009; Gómez et al. 2012) via the impact of tidally induced large-scale stellar density structures. We note, however, that the properties of the self-excited and tidally induced spirals (or bar) could be different, also implying a different impact on the kinematics of the stellar populations in the disk (Bland-Hawthorn & Tepper-García 2021).

The *Gaia* RVS sample (DR2) is the largest ever available sample of stars with 6D phase-space information. It enables identifying stellar overdensities corresponding to the spiral arms in angular momentum (or guiding) space (Khoperskov et al. 2020a). This makes it possible to constrain the physical locations of these stellar density structures in the Galactic plane. The analysis of angular momentum space sharpens the stellar overdensities by squeezing the stellar orbits towards their guiding centres, reducing the blurring by their epicyclic motions. The success of this idea is confirmed by (i) the good correspondence of the recovered large-scale stellar density structure with the location of spiral arms obtained with high-mass star formation regions (Reid et al. 2014), and (ii) the comparison with  $N$ -body and hydrodynamical simulations showing a similar rela-

tion between stellar angular momentum overdensities and their spirals arms.

The aim of this work is to explore the link between the MW spiral arms, the radially extended ridges in the  $(R, v_\phi)$  plane, and the numerous local moving groups in the SNd  $v_R$ - $v_\phi$  plane. We illustrate our findings in the MW with a parallel, comprehensive analysis of a new high-resolution  $N$ -body simulation of a MW-type spiral galaxy. The structure of the paper is the following. In Sect. 2 we explore various manifestations of the tightly wound spiral structure in the new simulations in the galactic plane, in  $(R, v_\phi)$  space, and in a SNd-like region. In Sect. 3 we define our sample of stars from *Gaia* DR2 and EDR3, and provide new evidence of the presence of the MW stellar spiral arms in the angular momentum (or guiding) space and their contribution to various phase-space features. Section 4 describes chemical abundance information from Galah (DR 3), APOGEE (DR 16), and LAMOST (DR 5), which we used to highlight signatures of the bar and spiral arms in these data. Finally, we discuss our results and summarize our findings in Sect. 5.

## 2. Simulated galactic disk with tightly wound spiral arms

### 2.1. Model description

In order to investigate *Gaia*-like phase-space features in a MW-type disk, we focus in this section on the analysis of a new, high-resolution  $N$ -body simulation of an isolated disk galaxy with a tightly wound, multi-arm spiral structure. We performed a single high-resolution,  $N$ -body simulation of a disk galaxy. The initial disk was represented by a Miyamoto-Nagai density profile (Miyamoto & Nagai 1975) with a characteristic scale length of 4 kpc, a vertical thicknesses of 0.15 kpc, and a mass of  $6 \times 10^{10} M_\odot$ . The simulation included a live dark matter halo whose density distribution followed a Plummer sphere (Plummer 1911) with a total mass of  $6.2 \times 10^{11} M_\odot$  and a scale radius of 21 kpc. This choice of parameters led to a galaxy mass model with a circular velocity of  $\approx 220 \text{ km s}^{-1}$ , but to facilitate comparison with MW kinematics, we rescaled our galaxy to have a circular velocity of  $240 \text{ km s}^{-1}$  near the solar radius at 8.2 kpc (Bland-Hawthorn & Gerhard 2016). The initial setup was generated using the iterative method provided in the AGAMA software (Vasiliev 2019).

In order to resolve substructures in the phase space, we used  $120 \times 10^6$  particles to model the stellar disk component and 61 451 200 particles to model the dark matter halo. This model has one of the highest resolutions of current  $N$ -body simulations of an isolated disk galaxy (see e.g. Fujii et al. 2019; Khoperskov et al. 2019; Asano et al. 2020). However, the number of particles in a SNd-like region in this high-resolution model is still lower by a factor of  $\sim 5$  than the number of stars already available in the *Gaia* RVS sample.

For the  $N$ -body system integration, we used our parallel version of the TREE-GRAPe code (Sect. 4.1 Fukushige et al. 2005) with multi-thread usage under the SSE and AVX instructions. We have used and extensively tested the hardware-accelerator-based gravity calculation routine in several galaxy dynamics studies and obtained accurate results with a good performance (see e.g. Saburova et al. 2017; Khoperskov et al. 2018a; Di Matteo et al. 2019a). In the simulation, we adopted the standard opening angle  $\theta = 0.5$  and a gravitational softening parameter equal to 4 pc. For the time integration, we used a leapfrog integrator with a fixed step size of 0.1 Myr.

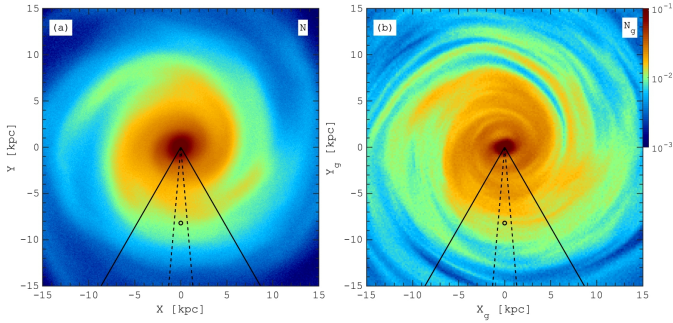


**Fig. 1.** Stellar density maps of the  $N$ -body model in  $(X, Y)$  (left) and  $(X_g, Y_g)$  coordinates (right, see Eq. (1) for the guiding coordinates transformation). The solid lines highlight a region of  $60^\circ$  in azimuth, comparable to the coverage in the MW of the *Gaia* RVS sample. The dashed lines limit the region we adopt in the analysis of  $R-v_\phi$ -ridges, and an SNd-like region (0.2 kpc, solid line circle) is placed at  $Y = -8.0$  kpc.

## 2.2. Angular momentum (guiding) space

The  $N$ -body model presented here is unstable towards the formation of a multi-arm, tightly wound spiral structure in the early phases of evolution, while a strong stellar bar, as in many MW models, forms at later times. To focus our analysis on the spiral arms, we considered a single snapshot at 880 Myr for which we extracted the particle positions and velocities that are used in the phase-space plots below. Figure 1a shows the stellar density map of this snapshot. The superposed solid lines highlight a cone region of  $60^\circ$  that is roughly comparable to the *Gaia* radial velocity sample coverage (with  $<10\%$  parallax error), the dashed lines show the region we adopted in the analysis of  $(R_g, v_\phi)$  ridges, and a 0.2 kpc radius SNd-like region is placed at 8.0 kpc from the centre, within which we explore the substructures (so-called moving groups) in simulated  $v_R-v_\phi$ -space.

Similar to our previous study (Khoperskov et al. 2020a), we present in Fig. 1b the global structure of the angular momentum space in Cartesian guiding coordinates defined as

$$X_g = R_g \cos(\phi), \quad Y_g = R_g \sin(\phi), \quad (1)$$

where  $R_g = L_z / (240 \text{ km s}^{-1})$  is the guiding radius of the particles,  $L_z = R \times v_\phi$  is the angular momentum,  $R$  is the instantaneous value of the galactocentric distance,  $\phi$  is the azimuthal angle in cylindrical coordinates, and  $v_\phi$  is the instantaneous value of the azimuthal velocity. In this notation, the guiding radii of stars correspond to the angular momentum normalised by the circular velocity beyond  $>4$  kpc in the disk. For near-circular orbits in an axisymmetric potential, in which  $L_z$  is conserved,  $R_g$  is the true time-independent guiding-centre radius. For more realistic potentials with non-axisymmetric perturbations,  $R_g$  can be thought of as an approximate orbit-averaged mean radius.

As shown in Khoperskov et al. (2020a), this approach allows us to decrease the effects of the radial oscillations of stars and detect phase-space overdensities in the disk that would otherwise be too blurred to see. The approximation of a constant circular velocity is reasonable for galaxies with a nearly flat rotation curve. Recent *Gaia* data analysis shows a gently declining rotation curve in the MW, for example, with a gradient  $-1.7 \pm 0.1 \text{ km s}^{-1} \text{ kpc}^{-1}$  in Eilers et al. (2019) and  $-1.41 \pm 0.2 \text{ km s}^{-1} \text{ kpc}^{-1}$  in Mróz et al. (2019). This corresponds to a change of  $\approx 2\%$  change in the derived guiding radii at 3 kpc from the Sun, which we neglect here for simplicity.

By transforming the in-plane coordinates of stars  $(X, Y)$  to  $(X_g, Y_g)$ , we used a simpler description than the full transfor-

mation to the action-angle variables of a nearby axisymmetric potential, whereby also the azimuthal blurring can be removed by transforming the star into the  $\theta_\phi$  conjugate to  $R_g$ . This procedure requires knowledge of the full gravitational potential, which we wish to avoid in view of the later application to the MW in Sect. 3. However, for the  $N$ -body model particles, we used the action-angle transformation in the epicyclic approximation (e.g., Monari et al. 2016a) to construct a map similar to the  $(X_g, Y_g)$  map in Fig. 1. However, the differences between the two maps are small. Moreover, we used the particle distribution in  $(X_g, Y_g)$  only for identification, and transferred back into  $(X, Y)$  before comparing with other  $(X, Y)$  information or data. Therefore the exact transformation used to reduce the epicyclic blurring is not important.

The map of the particle distribution resulting from the coordinate transformation of Eq. (1) is compared to the original density distribution in Fig. 1. In the original density map, the spiral structure is represented by two to three main large-scale and broad arms. In contrast, the density distribution in the guiding coordinates shows multiple narrow and tightly wound density structures. Some of these overdensities in Fig. 1b evidently correspond to the main spiral arms in Fig. 1a, but as expected, they are more concentrated in radius. A few less prominent overdensities in Fig. 1b are faintly seen in the left panel, while others do not seem to match any structure in  $(X, Y)$  space. No direct match of the density structures in  $(X, Y)$  and  $(X_g, Y_g)$  coordinates is expected because the spiral pattern, while tightly wound, is not axisymmetric, nor is the gravitational potential. However, an exact match is not needed; similar as in Khoperskov et al. (2020a), when stars in the  $(X_g, Y_g)$  overdensities were identified, we back-transformed, determined the corresponding features in  $(X, Y)$  space, and compared with the physical spiral arms.

## 2.3. N-body model: Overdensities in angular momentum (guiding) space

We start our analysis by providing a more detailed description of the angular momentum space. Figures 2a, c show unsharp-masked angular momentum density distributions in polar  $(R_g, \phi)$  coordinates, defined as

$$\delta N_g(R_g, \phi) = [N_g(R_g, \phi) - \langle N_g(R_g, \phi) \rangle] / \langle N_g(R_g, \phi) \rangle, \quad (2)$$

where  $\langle N_g \rangle$  denotes the mean number density map constructed by convolving the density distribution with a 2D Gaussian kernel with a width of 500 pc. The large-scale map in Fig. 2a shows a large number of radially extended overdensities with an amplitude of up to 20%. In the local, *Gaia*-like region illustrated in panel c, these overdensities are visible as a more nearly vertically extended (along azimuth) wave-like pattern. These maps and Figs. 2b,d, which shows corresponding mean radial velocity distributions, can be compared to similar maps based on the *Gaia* radial velocity sample presented in Friske & Schönrich (2019) and Monari et al. (2019b). On large scales, see Fig. 2b, we find a symmetry of almost  $180^\circ$  of the  $v_R(R_g, \phi)$  velocity distribution (see also Chiba et al. 2021), likely caused by the central oval (proto-bar in the model). On top of the large-scale pattern, we observe multiple sharp velocity wave-like modulations (see also Friske & Schönrich 2019). Interestingly, these radial velocity oscillations are tightly connected to the density variations (see Figs. 2a, c). For instance, comparison of panels c and d implies that overdensities ( $\delta N_g > 0$ ) generally correspond to the more negative radial velocity regions, which can be explained when the stellar overdensities in the

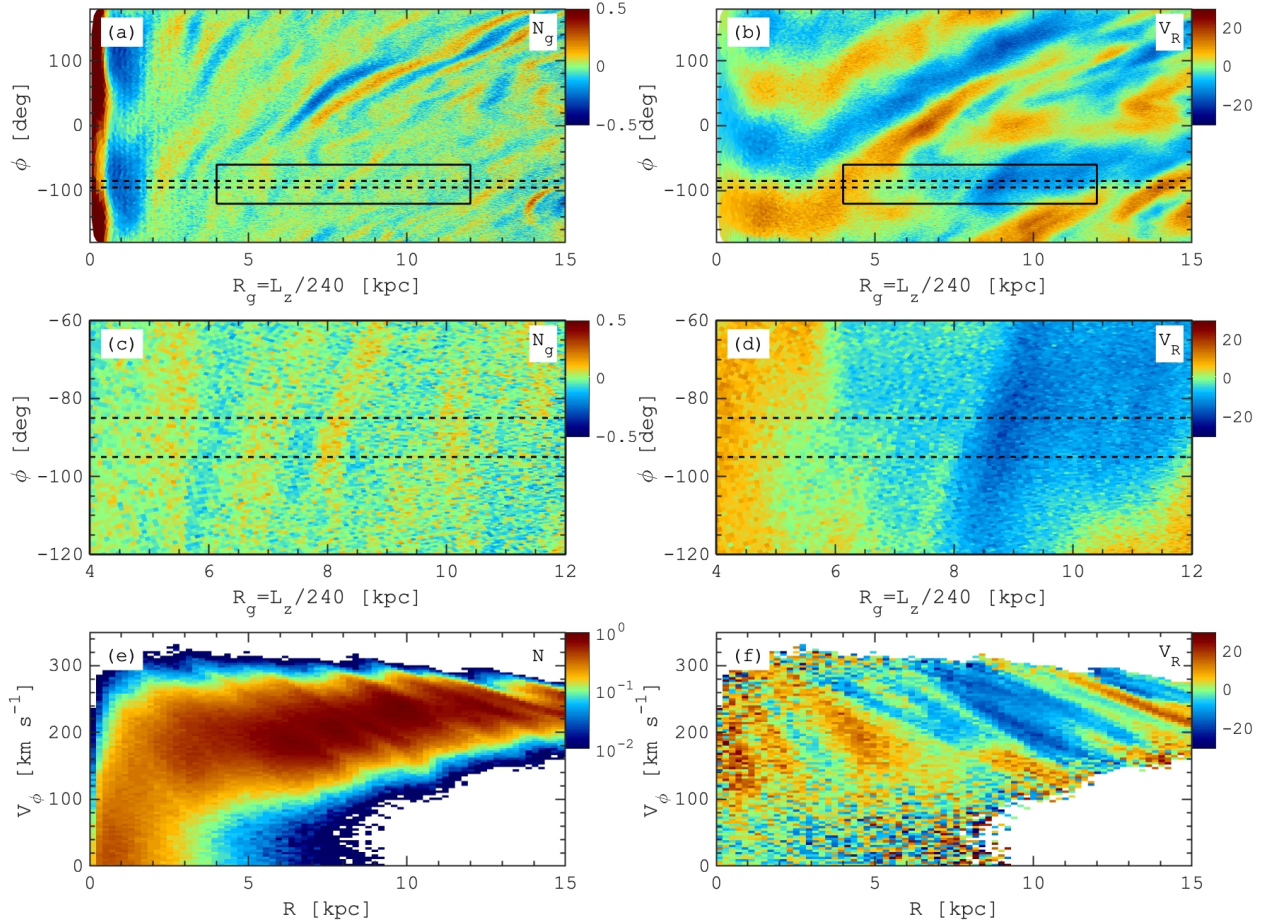


**Fig. 2.** Analysis of the guiding space of the  $N$ -body model. *Top row:* unsharp-masked stellar density distribution in the  $N$ -body simulation (a) and the mean radial velocity map (b) in the  $(R_g, \phi)$ -plane. *Middle row:* zoomed maps of the rectangular region indicated in the top row: density perturbation (c), and the mean radial velocity map (d). *Bottom row:* density (e) and the mean radial velocity (f) in the  $(R, v_\phi)$  coordinates for all stars in a narrow azimuthal strip, indicated by the dashed lines in the top and middle rows.

guiding space contain stars associated with tightly-wound spiral arms (Siebert et al. 2012; Faure et al. 2014; Antoja et al. 2016).

Next, Fig. 2e shows the  $(R, v_\phi)$  plane for particles selected in a narrow  $10^\circ$  region. Similar to a number of previous studies, we observe so-called ridges, that is, radially extended (3–5 kpc long) diagonal stellar overdensities roughly corresponding to constant angular momentum. The map in Fig. 2f depicts the radial velocity variations associated with these density ridges. The global structure and the amplitude of the velocity pattern (15–30 km s<sup>-1</sup>) is similar to that found in the MW with *Gaia*-RVS (see e.g. Fragkoudi et al. 2019; Laporte et al. 2019).

Having seen that our model is qualitatively similar to the MW disk kinematics seen in *Gaia*-RVS, we now explore the origin of the  $(X_g, Y_g)$  overdensities and their connection to the model spiral arms further. Because of the exponential radial density profile in the model, the contrast of the spiral arms in a colour map such as Fig. 1a is low; for a more precise description, we therefore used an unsharp-masked map of the  $(X, Y)$  stellar density distribution; see Fig. 3a. This map indeed depicts a multi-armed, tightly wound spiral pattern, in which some of the arms (overdensities with  $\delta N > 0$ ) can be traced over  $360^\circ$  in azimuth. The amplitudes of the spiral arms do not exceed 10–20% and also vary along the individual arms.

Next to this figure, we show the unsharp-masked density map in the guiding  $(X_g, Y_g)$  coordinates (Fig. 3b). Interestingly, the global morphology of the density perturbation is similar in both

maps, but the guiding space overdensities are more radially concentrated and thus can have larger amplitudes (up to  $\delta N_g \approx 0.4$ ), and several of them apparently can map to one broader spatial spiral arm. The higher concentrations and amplitudes are easily understood because the coordinate transformation of Eq. (1) moves stars close the mean radial location, thus enhancing the amplitude of angular momentum structures in a given azimuthal range. The peak angular momentum corresponding to a certain overdensity varies with azimuth, which is clearly visible over large angular scales in Fig. 2a, but to a lesser degree, also on smaller scales (Fig. 2c).

Without making explicit connections between particular structures in  $(X_g, Y_g)$  and  $(X, Y)$ , we can establish a global correspondence between the overdensities in the guiding coordinates and the real-space stellar overdensities: Fig. 3c shows the  $(X, Y)$  density map obtained by summing the contributions of all back-transformed particles from the  $(X_g, Y_g)$  distribution, but weighted by the amplitude of the  $\delta N_g$  perturbation in Fig. 3b. The multiple structures in panel c nicely trace the large-scale locations of the spiral arm overdensities in panel a, showing that the peaks in the angular momentum distribution of this model are related to the positive spiral density perturbation in  $(X, Y)$  space, even if one apparent density arm may contain more than one blurred angular momentum peak.

Next we focus on a smaller region in the simulated galaxy, similar to that covered by the *Gaia* data, to illustrate the

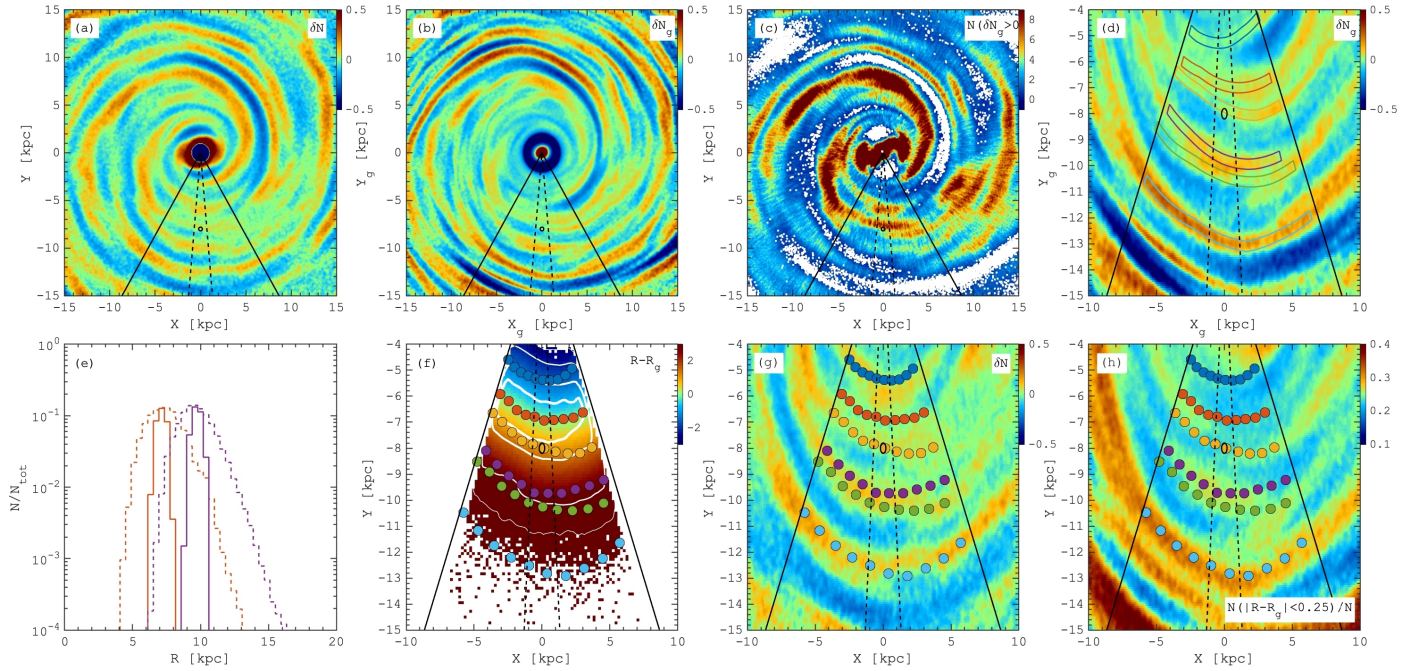


**Fig. 3.** Properties of spiral arms in the  $N$ -body simulation. (a): unsharp masking of stellar density in the galaxy ( $X, Y$ ) plane, showing a density perturbation of the tightly wound spiral arm. (b): unsharp-masked stellar density distribution in guiding ( $X_g, Y_g$ ) coordinates. (c): density distribution of stars in ( $X, Y$ ), weighted by the positive density perturbation at their corresponding ( $X_g, Y_g$ ) coordinates. (d): background map is a zoom-in of (b); coloured lines indicate the  $\pm 200$  pc wide radial selection regions along the peaks of the distribution in this map. (e): distributions of galactocentric radii for all stars in two ( $X_g, Y_g$ ) selection regions (the second overdensity is shown in red, and the fourth overdensity is plotted in purple as dashed lines). Solid lines correspond to the subset of stars that are located close to their guiding radii,  $|R - R_g| < 0.25$  kpc. (f): background scatter plot shows the ( $X, Y$ ) positions of all particles in the second (red) ( $X_g, Y_g$ ) overdensity region, where the white contours correspond to 0.8, 0.5, 0.1, and 0.01 density levels. Filled circles show the locations of density maxima as illustrated in (panel e) for all overdensities marked in (panel d). (g): correspondence between the density perturbation of the spiral arm (zoom-in from panel a) and the location of such density maxima corresponding to all overdensities selected in ( $X_g, Y_g$ ) (panel d). (h): background map represents the fraction of stars in ( $X, Y$ ) coordinates near their guiding centres (dynamically cold population with  $|R - R_g| < 0.25$ ), and the filled circles show the location of the same density maxima as in (panels f and g).

connection between particular guiding space overdensities and the corresponding spiral arms in Fig. 3a in more detail. Figure 3d zooms in on the lower part of panel b, highlighting the guiding space overdensities by the coloured bands. These bands contain stars located within regions of  $R_g \pm 200$  pc near the peaks of the overdensities. In Fig. 3e, the dashed lines show the number of stars as a function of galactocentric distance for the second (red) and the fourth (purple) angular momentum overdensities. Stars from both overdensities span a very large radial range,  $\sim 6$ – $7$  kpc, with significant overlap between them. Clearly, stars from several other ( $X_g, Y_g$ ) overdensities will also overlap with these two; this is illustrated in Figs. 3e,f.

To characterise the amplitude of the orbital oscillations, we calculated the difference between current galactocentric distance and guiding radius  $R - R_g$ . This parameter represents an average radial excursion of stars because even though stars with large radial oscillations can be found near their guiding centres, the probability of this is low, while dynamically cold stars always stay near their guiding centres. According to Fig. 3c, a guiding space overdensity should mainly contain stars with low  $|R - R_g|$  near its peak, while the tails of the  $|R - R_g|$  distribution should be populated by hotter stars. This is illustrated in Fig. 3e, where the solid lines represent the radial distribution of stars with low mean  $|R - R_g| < 0.25$  kpc. For two (red and purple) overdensities, these distributions are narrow and located near the maxima of the density distributions for all  $|R - R_g|$  (dashed lines). In panel f of Fig. 3, the scatter plot depicts the ( $X, Y$ ) distribution of stars from

one of the aforementioned overdensities (red one), colour-coded by the value of  $|R - R_g|$ . Large filled circles correspond to the location of density maxima similar to those illustrated in panel e for all overdensities marked in panel d. Although the selection stripes in panel d have similar shapes to those traced by the fitted density maxima (circles in panel f), these structures are not the same because the latter represent the mean locations of stars in ( $X, Y$ ) coordinates for a given overdensity in ( $X_g, Y_g$ ).

Finally, after identifying the ( $X_g, Y_g$ ) locations of the stellar density structures for the angular momentum overdensities, we compare them in Fig. 3g with the spiral arm density perturbations (zoom in of map in panel a), where the filled circles are the same as in panel f. The locus of stars selected near the peaks of the guiding centre map clearly correspond well to the real spiral arms. This agreement parallels our previous finding (Khoperskov et al. 2020a) with the same procedure as described here, that the density maxima of MW stars selected in the angular momentum (or guiding ( $X_g, Y_g$ )) space overdensities match the locations of high-mass star-forming regions used as tracers of the MW spiral arms. Figure 3 shows that in our high-resolution simulation, single guiding space overdensities dominate individual spiral arms. However, this does not rule out the possibility that depending on the dynamical nature of the spiral arms, several such overdensities in other simulations contribute substantially to a single arm (see e.g. Hunt et al. 2020). In this case, the  $XY$ -locus of the guiding space overdensities would overlap, which we did not observe in the available *Gaia*

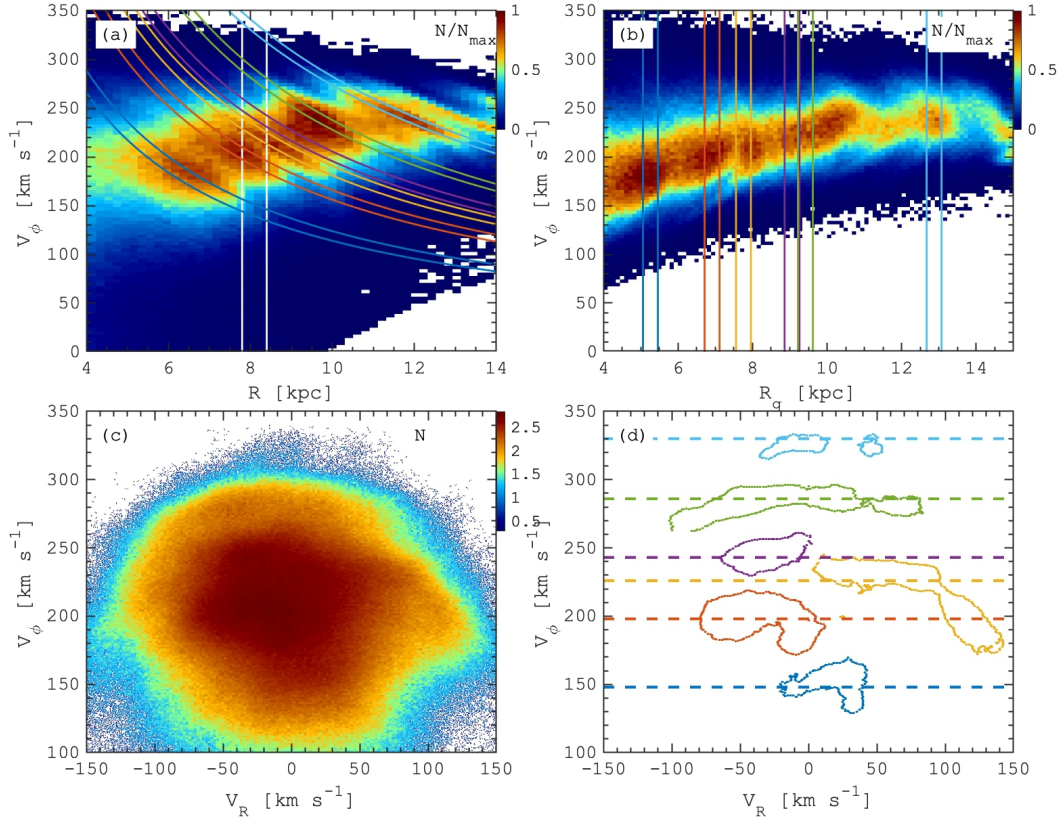


**Fig. 4.** Relation between diagonal ridges and the moving groups in  $N$ -body simulation. (a): density distribution in the  $(R, v_\phi)$  plane for stars selected in a  $10^\circ$  azimuthal cone (see Fig. 3). Coloured lines represent the selected spiral arm regions in guiding coordinates (see Fig. 3d). White vertical lines limit the SNd-like region at  $8 \pm 0.2$  kpc. (b): same as in (a), but transformed into  $R_g$ - $v_\phi$  coordinates. (c): phase-space  $(v_R, v_\phi)$  density contours for stars in the SNd-like region between the white lines in (a). (d): coloured density contours highlight the positive overdensities in  $(v_R, v_\phi)$  coordinates after unsharp masking of the density distribution in (c). The colours of the  $(v_R, v_\phi)$  overdensities are chosen to match the angular momentum (guiding radius) of the large-scale selections made in  $(X_g, Y_g)$  (see Fig. 3d) and thus provide correspondence between the local SNd-like  $(v_R, v_\phi)$  features and large-scale  $(R, v_\phi)$  ridges shown in (panel a).

data (Khoperskov et al. 2020a), at least for the most prominent features. This issue could be further tested with forthcoming *Gaia* releases.

Another approach for locating the spiral arms in this model is shown in panel h of Fig. 3 (see also panel e), where the density maxima of the spiral arms also correspond to maxima in the fraction of stars near their guiding centres. Specifically, a map of the fraction of stars with  $|R - R_g| < 0.25$  is shown together with the same filled circles in panels f and g, which represent the mean locations of the spiral arms in  $(X, Y)$ . The spiral arms correspond well with a higher fraction of dynamically cold stars. This suggests that we can trace the mean locations of the MW spiral arms in *Gaia* data as well by finding the regions with a larger fraction of stars with low  $|R - R_g|$  (see Sect. 3.1). A larger fraction of stars with cold orbits near the spiral arms does not necessarily suggest that these stars formed locally in the arms. These dynamically cold disk populations likely react more efficiently than kinematically hot stars to gravitational perturbations of the spiral arms (see e.g. Khoperskov et al. 2018b).

#### 2.4. Linking the spiral arms with $R$ - $v_\phi$ -ridges and the $v_R v_\phi$ space in the $N$ -body simulation

In the previous section, we identified the location of tightly wound spiral arms in our  $N$ -body model by using the overdensities in the guiding (or angular momentum) coordinates. One

of the most exciting properties of the spirals is the large radial spread of the stars associated with individual arms (see panels e and f in Fig. 3). In this section, we discuss the manifestations of this behaviour in different phase-space projections that are well studied in the MW. In particular, we quantify the contribution of the spiral arms to the  $(R, v_\phi)$  structures across the Galactic disk and in the local  $v_R$ - $v_\phi$  space, which has been intensively explored in the SNd over the past decades (see references in the Introduction).

In Fig. 4 we present the analysis of  $(R, v_\phi)$  space taken in a narrow  $10^\circ$  azimuthal cone selection (see dashed lines in Figs. 1–3) and the  $v_R$ - $v_\phi$  space selected in between  $R = 8 \pm 0.2$  kpc in this region. As we noted in the previous section, the  $(R, v_\phi)$  space includes a large number of diagonal overdensities, the ridges, which span over 3–7 kpc across the Galaxy. To investigate the relation with the spiral arms as in the previous section, we overplot the contours reflecting our angular momentum selections (see panel d in Fig. 3). They clearly coincide well with the  $(R, v_\phi)$  density ridges. In Fig. 4b we also show the  $(R_g, v_\phi)$  space in which the diagonal ridges are transformed into nearly vertically aligned overdensities, which in fact depict the azimuthal velocity structure of the  $(X_g, Y_g)$  overdensities. Similar to the previous panel, we highlight by contours our angular momentum selections, in which the radially extended kinematical structures and the spiral arms clearly agree in the  $N$ -body simulation. In contrast to the  $(R, v_\phi)$  space, the different structures do not overlap here, which shows why it is

convenient to identify the underlying structures in angular momentum space.

In the MW, the diagonal density ridges discovered with GRV2 pass through the solar vicinity, and thus, as shown in several recent works (Ramos et al. 2018; Quillen et al. 2018; Martinez-Medina et al. 2019; Fragkoudi et al. 2019), they may contribute to the known moving groups in  $v_R$ - $v_\phi$  space. In our simulation, we arbitrarily set up a SNd-like region at  $8 \pm 0.2$  kpc shown with white lines in Fig. 4a. In Fig. 4c we show the corresponding density distribution in  $v_R$ - $v_\phi$  coordinates. A clearer picture of the velocity structures is shown in Fig. 4d, where we show zero-levels of the main overdensities derived by applying unsharp masking to the number star counts (panel c). This plot clearly shows a number of features with an arch-like shape, similar to those found in the SNd (Gaia Collaboration 2018a). A match between the  $v_R$ - $v_\phi$  overdensities and particular  $(R, v_\phi)$  ridges (and thus underlying spirals) can be made by comparing their mean azimuthal velocities. For the  $(R, v_\phi)$  ridges in the SNd-like region, these are shown by horizontal dashed lines. The colour of the  $v_R$ - $v_\phi$  overdensities is taken to be same as the colour of the nearby angular momentum selection. This demonstrates a perfect match between the ridges and the main  $v_R$ - $v_\phi$  overdensities. In particular, we can identify the contribution of all six stellar density structures. Keeping in mind that these ridges correspond to the spiral arms, we suggest that stars tracing the inner disk spirals can be found in the bottom part of the  $v_R$ - $v_\phi$  plane (below LSR), while the outer disk spiral arms are imprinted at the top of the distribution. For example, the highest- $v_\phi$  velocity  $v_R$ - $v_\phi$  features (green and light blue) correspond to spiral arms with a locus well beyond 8 kpc.

We demonstrated that in our  $N$ -body simulation, tightly wound spiral arms correspond to radially extended stellar density structures that have higher contrast in the distribution of the guiding radii. The radial extension of the spiral arms leads to their appearance at different galactocentric radii, causing prominent features in the  $(R, v_\phi)$  plane, which in turn contribute to the substructures in  $v_R$ - $v_\phi$  space at a certain galactic radius. The many similarities of the disk kinematics in this simulation with the *Gaia* data then suggest that a number of kinematic arches (or moving groups) in the SNd  $v_R$ - $v_\phi$  plane may similarly be associated with the MW spiral arms.

### 3. MW phase-space

In this section, we explore the structure and kinematics of stars in the SNd  $v_R$ - $v_\phi$  space,  $(R, v_\phi)$  coordinates, and in the Galactic plane using *Gaia* data. We indicate how the most prominent phase-space features are linked to the MW stellar density structures (spiral arms and main bar resonances). We use the dynamical structure found in our  $N$ -body simulation as a guide to determine the correlations between in-plane overdensities in the guiding coordinates and the diagonal ridges and moving groups.

*Gaia* (EDR3+DR2) is the largest available 6D phase-space dataset for  $\approx 7.2$  million stars brighter than  $G_{\text{RVS}} = 12$  mag. It enables possible precise studies of the MW structure on large scales and tracing the kinematics of the disk across multiple kiloparsecs around the Sun. For this work, we first took all sources with an available five-parameter astrometric solution (sky positions, parallaxes, and proper motions) from *Gaia* EDR3 (Lindgren et al. 2021a) and radial velocities from *Gaia* DR2 (Gaia Collaboration 2018b). From this sample (hereafter G3RV2), we selected stars with positive parallaxes and relative errors on parallaxes smaller than 10%. We

estimated the parallax zero-point as a function of magnitude, colour, and ecliptic latitude by using the routine that is available as part of the *Gaia* EDR3 access facilities (Lindgren et al. 2021b)<sup>1</sup>. Additionally, we took the median parallax of the quasars of  $-17 \mu\text{s}$  into account (Lindgren et al. 2021b). Distances were computed by inverting parallaxes. To calculate positions and velocities in the galactocentric rest-frame, we assumed an in-plane distance of the Sun from the Galactic centre of 8.19 kpc (GRAVITY Collaboration 2018), a velocity of the local standard of rest,  $v_{\text{LSR}} = 240 \text{ km s}^{-1}$  (Reid et al. 2014), and a peculiar velocity of the Sun with respect to the LSR,  $U_\odot = 11.1 \text{ km s}^{-1}$ ,  $v_\odot = 12.24 \text{ km s}^{-1}$ , and  $W_\odot = 7.25 \text{ km s}^{-1}$  (Schönrich et al. 2010).

#### 3.1. MW spiral arms in the G3RV2

First we present the angular momentum (or guiding space) distribution for the G3RV2 stars. Different from our previous work, we did not apply the homogenisation of the density distribution (see Fig. 1 in Khoperskov et al. 2020a). We assumed a constant value of the circular velocity  $v_c = 240 \text{ km s}^{-1}$  to compute the guiding radii of the stars; as discussed in Sect. 2.2, this is a good approximation. In Fig. 5 we show the density distribution and its unsharp masking in the guiding polar  $(R_g, \phi)$  coordinates for better comparison with some recent works (Monari et al. 2019b; Friske & Schönrich 2019; Chiba et al. 2021). The density distribution reveals several notable structures seen as azimuthally extended tightly wound trailing overdensities. The unsharp masking allows us to highlight six main structures that are prominent across the entire G3RV2 sample. These overdensities overlap with the radial velocity pattern (right panels), first discovered in Schönrich & Dehnen (2018) and discussed also in Friske & Schönrich (2019), who interpreted the complex velocity pattern as the manifestation of the spiral structure. More recently, Wheeler et al. (2021) suggested that some of the angular momentum overdensities can be associated with the main resonances of the MW bar (see also Monari et al. 2019a).

Because the G3RV2 dataset, while covering a large area in the MW, is still dominated by the stars in the extended solar vicinity, it is important to test to which extent the density-velocity patterns we observe are caused by the local stars. In the bottom panels of Fig. 5, we show exactly the same maps as in the top panels, but for stars located outside 1 kpc from the Sun. Obviously, the density distribution and its unsharp masking are now significantly impacted by our selection, but they still reveal the main stellar density structures in the unsharp mask. In particular, the radial velocity map is almost identical to that based on the entire G3RV2, implying that the stellar density structures in the angular momentum space cannot be explained by local stars (or by selection or extinction biases). This does not support the possibility discussed in the recent study by Hunt et al. (2020), that the overdensities in  $(X_g, Y_g)$  we found in Khoperskov et al. (2020a) are generated by the local  $v_R$ - $v_\phi$  moving groups because the G3RV2 sample is dominated by stars in the SNd. Although the large majority of stars in the G3RV2 sample can indeed be found close to the Sun, the distant ( $D > 1$  kpc) stars in Fig. 5 show patterns that are very similar to those of the full sample.

From Fig. 5 we conclude that similar to our  $N$ -body simulation, the MW angular momentum space is not featureless, but contains the imprint of a number of overdensities that in the simulation represent the tightly wound spiral arms, although

<sup>1</sup> [https://gitlab.com/icc-ub/public/gaiadr3\\_zeropoint](https://gitlab.com/icc-ub/public/gaiadr3_zeropoint)

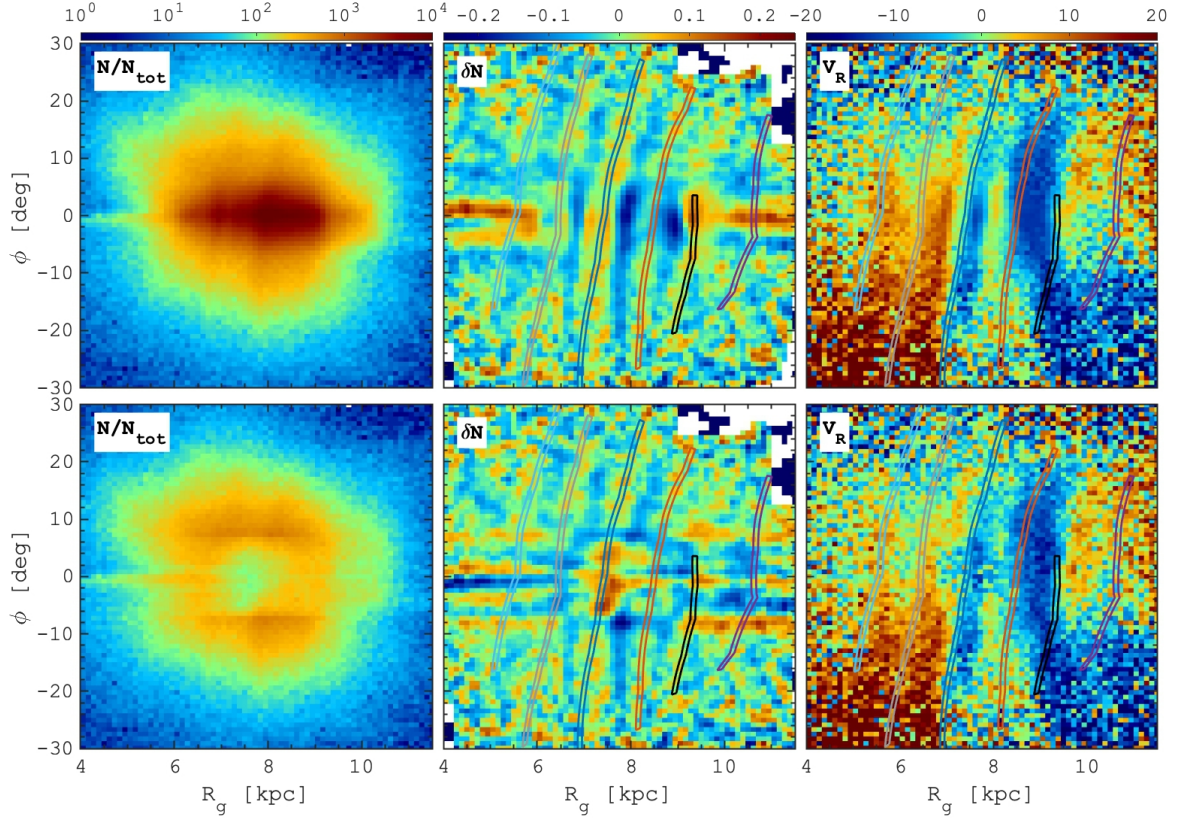


**Fig. 5.** Angular momentum (or guiding space) structure of the G3RV2 stars near the Galactic plane ( $|z| < 200$  pc): number of stars (*left*), unsharp masking of the density distribution (*centre*), and the mean radial velocity (*right*). *Bottom row*: the same, but for stars outside the SNd (at a cylindrical distance beyond 1 kpc from the Sun). Coloured lines depict the angular momentum selections that were used in  $(X_g, Y_g)$  coordinates to identify overdensities in [Khoperskov et al. \(2020a\)](#). The hole in the density distribution ( $R_g \approx 7.6$  kpc) in the *bottom left panel* is shifted towards the Galactic centre because the SNd contains more stars from the inner regions.

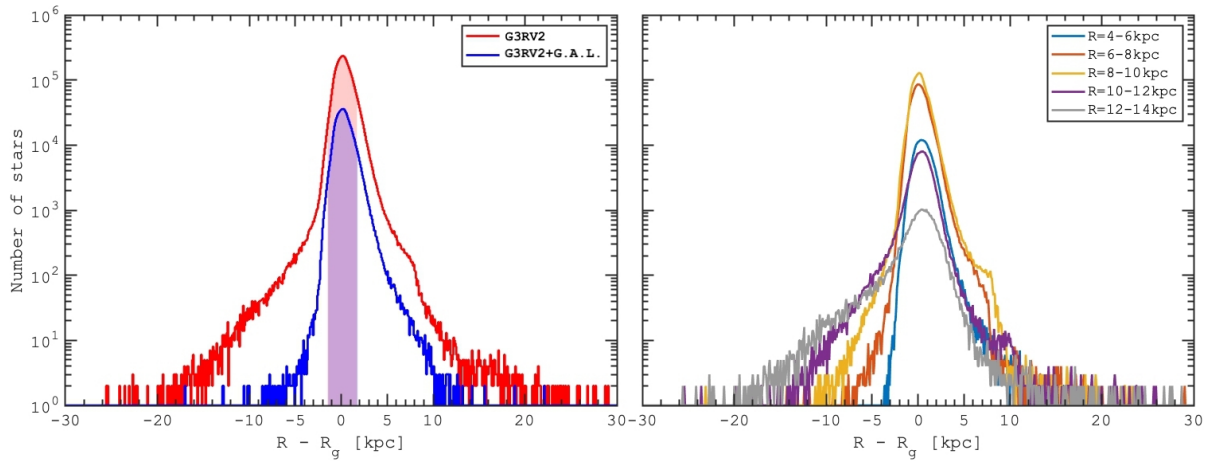


**Fig. 6.** Distribution of the difference between the current galactocentric position of stars and their guiding centres for the G3RV2 sample (red) and G3RV2 all stars in common with Galah, APOGEE, and LAMOST (GAL, blue; see Sect. 4) (*left*). Distribution of  $R - R_g$  for G3RV2 stars at different galactocentric radii (*right*). Shaded areas in the left panel correspond to 95% of the distribution around its maxima. The distributions suggest that most stars are found less than 2 kpc away from their guiding centres. The visible asymmetry of the distribution is caused by the contribution of accreted onto the MW stars (see Sect. 3.1 and Appendix A for details).

in [Khoperskov et al. \(2020a\)](#), we already showed that the *Gaia* DR2 (RVS) angular momentum overdensities are made of stars in the spiral arms and the main bar resonances. Here we use another approach; we recall that in the model (see Fig. 3h), the fraction of stars near their guiding centres (cold orbits stars) clearly highlight the location of the spiral arms. Using the same

idea for the MW, we show in Fig. 6 the global distribution of  $R - R_g$  for all stars in G3RV2. The shaded areas in the left panel show that 95% of the stars are located within  $\approx 2$  kpc away from their guiding centres. The visible asymmetry of the distributions is caused by the contribution of stars that are accreted onto the MW (see the end of this section and Appendix A for details).

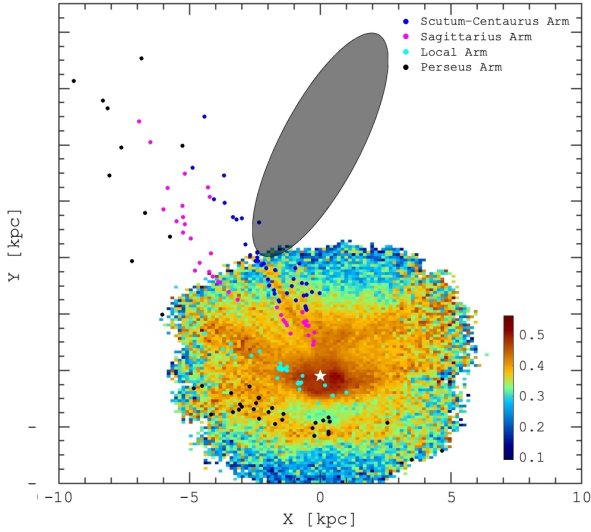


**Fig. 7.** Fraction of G3RV2 stars with  $|R - R_g| < 0.25$  kpc. The coloured points correspond to the location of the high-mass star-forming regions from Reid et al. (2019) associated with Scutum-Centaurus (blue) and Sagittarius (magenta) and the Local (cyan) and Perseus (black) arms. A star symbol corresponds to the location of the Sun, and the grey oval represents the orientation of  $\approx 4.6$  kpc long Milky Way bar (Wegg et al. 2015).

In Fig. 7 we present the fraction of stars located near their guiding centres ( $|R - R_g| < 0.25$  kpc) with an approximate location of the bar (grey oval) and the maser sources with  $< 10\%$  distance error (Reid et al. 2019) that are associated with the four MW spiral arms (Scutum-Centaurus (blue), Sagittarius (magenta), Local (cyan), and Perseus (black)). We did not involve the coordinate transformation and show the distributions in the real physical space. The distribution of stars near their guiding centres show three large-scale regions that match the locations of the maser sources in the spiral arms well. In particular, we find good agreement for the Perseus and Local arms, while the Sagittarius arm is less evident, but still visible in G3RV2. Our new approach fails only for the innermost Scutum-Sagittarius arm, where the stellar overdensity also overlaps with the masers, but does not represent a continued structure. Nevertheless, the approach of identifying of the spiral arms through the distribution of the dynamically cold stars provides good results in both the  $N$ -body model of the tightly wound spiral galaxy and in the MW (see recent finding by Poggio et al. 2021).

An interesting feature is the second component in the distributions at  $R - R_g \gtrsim 5$  kpc in Fig. 6. Obviously, these stars exhibit rotation in the opposite direction compared to the MW disk. By checking the kinematics and spatial distribution of these stars, we found that the vast majority of them show halo-like kinematics and therefore represent both accreted and heated populations (see e.g. Belokurov et al. 2018, 2020; Di Matteo et al. 2019b). Although this is beyond the scope of the paper, in Appendix A we confirm this finding using chemical abundance information in the  $[\alpha/\text{Fe}] - [\text{Fe}/\text{H}]$  plane.

### 3.2. Connection of $R - v_\phi$ ridges with the SNd $v_R - v_\phi$ structure in the MW

Next we focus on the radial structure of the MW spiral arms that is directly presented in Fig. 7 and the connection of the spiral arms to the stellar overdensities in Fig. 5. Similar to the simulation analysis, in Fig. 8 we show the radial distribu-

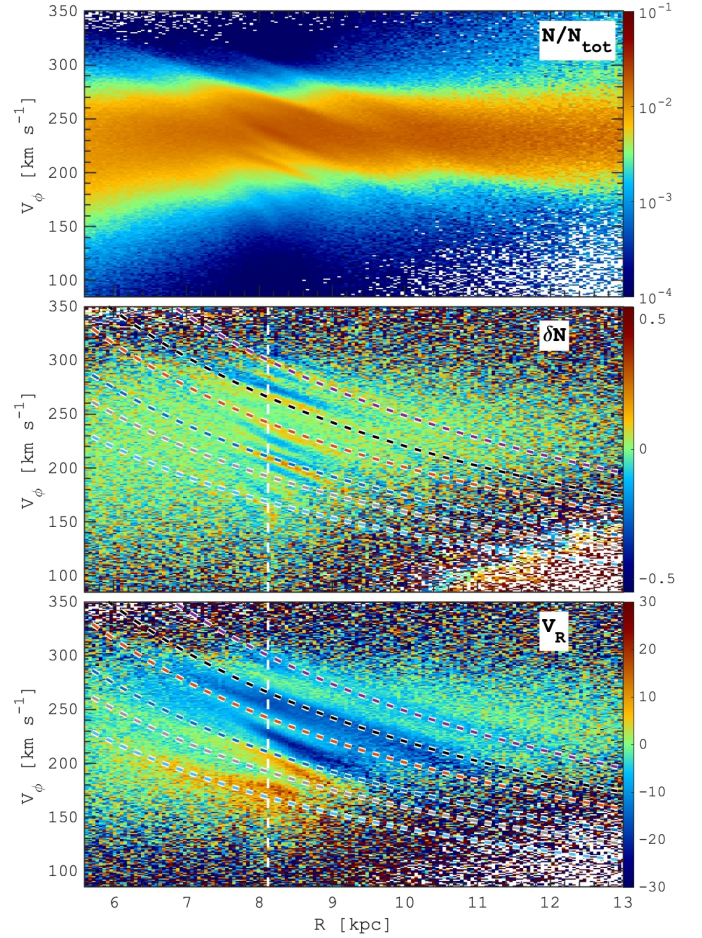


**Fig. 8.** Azimuthal velocity component structure in a narrow region  $\pm 5^\circ$  along the Galactic radius. *Top panel:* the density of stars normalised at each galactocentric distance. *Middle panel:* unsharp masking of the density distribution. *Bottom panel:* same distribution, but colour-coded by the mean radial velocity. Coloured diagonal lines depict the angular momentum selections in a given azimuthal range, using  $(X_g, Y_g)$  coordinates to identify the overdensities in Khoperskov et al. (2020a) (see also Fig. 5).

tion of azimuthal velocities for the G3RV2 stars selected in a narrow region ( $10^\circ$ ) along the galactocentric distance vector through the solar position. In order to highlight the stellar overdensities, we normalise the stellar density distribution at each radius separately (Fig. 8 top) and also present an unsharp-masking residual map (Fig. 8 middle) where several diagonal  $(R, v_\phi)$  ridges are now even more prominent (see e.g. also Antoja et al. 2018; Fragkoudi et al. 2019; Bland-Hawthorn et al. 2019). Despite the density normalisation, the ridges are still most prominent close to the SNd. Moreover, when we colour-code the  $(R, v_\phi)$  map by the mean radial velocity, the density ridges (see the unsharp-masking map) coexist, and the wave-like velocity pattern extends across the whole radial range available with G3RV2. This suggests that the real extensions of the density ridges are much larger than we observe in the density map. We expect that  $(R, v_\phi)$  ridges will be more prominent when the MW disk coverage is increased in the forthcoming *Gaia* releases (DR3 and DR4; see also recent EDR3 results for the outer MW disk; Gaia Collaboration 2021b).

To match the  $(R, v_\phi)$  ridges and overdensities in  $(X_g, Y_g)$ , we show the lines of a constant angular momentum corresponding to the mean stellar density structures in the guiding coordinates (see

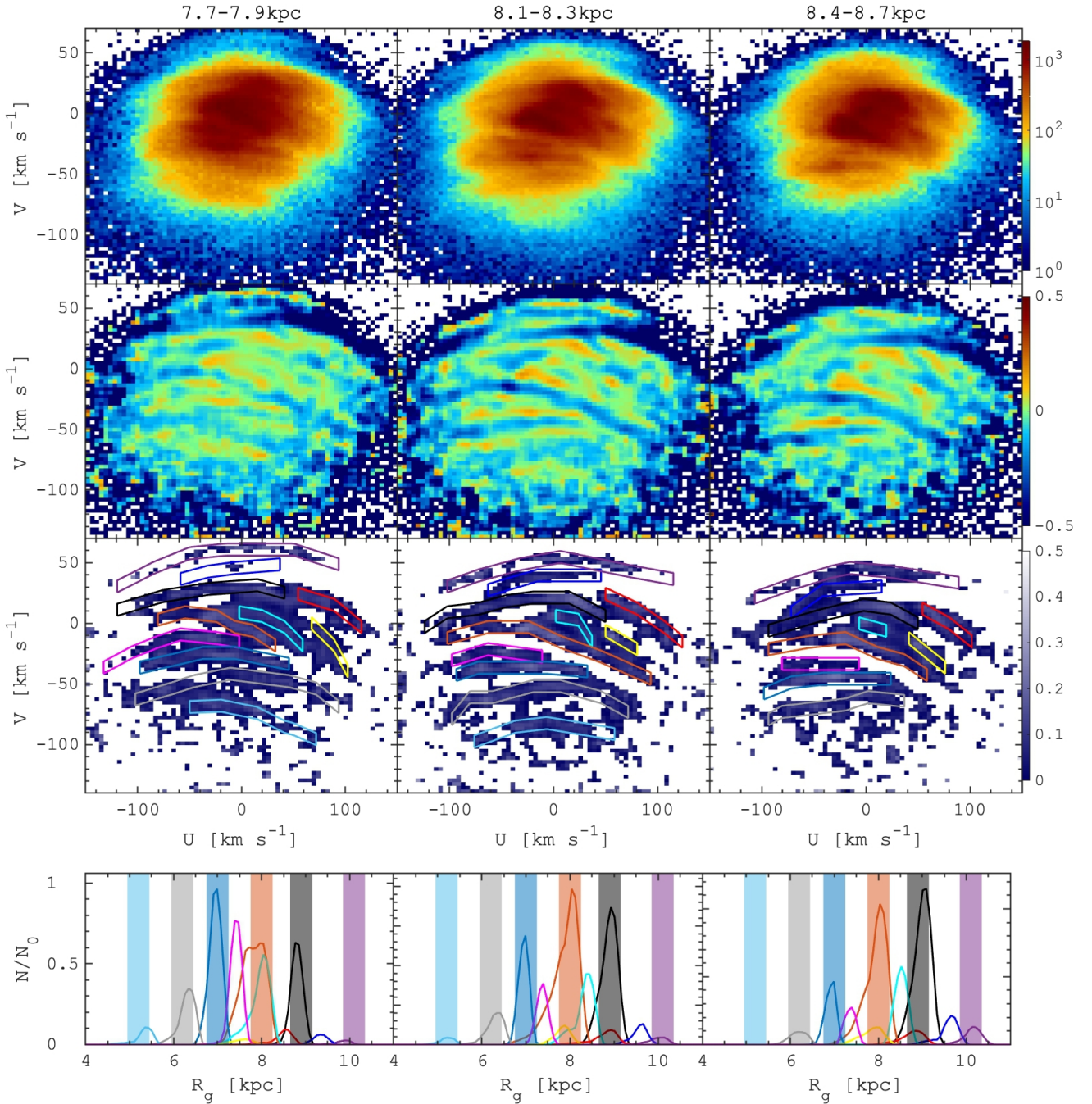


**Fig. 9.** Matching local  $v_R$ - $v_\phi$  features in the SNd with large-scale stellar overdensities in the guiding space of the MW. *First row:* number density of stars in kinematic  $v_R$ - $v_\phi$  space for the G3RV2 stars selected in three regions along the galactocentric radius:  $R = 7.8$  kpc (left),  $R = 8.2$  kpc (centre),  $R = 8.55$  kpc (right). Colour depicts the number of stars in log-scale. *Second row:* unsharp-masking maps (see Eq. (2)) for corresponding density distributions. *Third row:* positive part of the unsharp-masking maps (overdensities), where coloured boxes highlight different isolated kinematic overdensities. *Fourth row:* number of stars from each  $v_R$ - $v_\phi$  plane selected feature as a function of their angular momentum (or guiding radius). Coloured boxes depict the angular momentum selections used in  $(X_g, Y_g)$  coordinates to identify the main spiral arms of the MW, which coincide with known star-forming regions, and the bar resonances from Khoperskov et al. (2020a). In particular, the Arcturus stream (light blue) is a low-velocity tail of the Scutum-Centaurus spiral arm; part of the Hercules stream (grey) corresponds to the bar corotation, while its top part is likely to be the Sagittarius arm (blue); the Sirius stream represents the bar OLR (black); and the Hat is likely the high-velocity tail of the Perseus arm (purple).

Fig. 5 and in Khoperskov et al. 2020a) or colour bands in Fig. 5. In Fig. 8 the location of the density ridges agrees with the mean angular momentum of stars in  $(R_g, \phi)$  overdensities calculated in the same azimuthal range ( $<10^\circ$ ). Similar to the  $N$ -body model discussed above, we see a significant radial extension of the main stellar density structures across the large area in the MW

which can be traced along  $(R, v_\phi)$  with nearly constant angular momentum.

Finally, we take an in-depth look at the  $v_R$ - $v_\phi$  space in three regions along the Galactic radius with high coverage by G3RV2. In Fig. 9 (top) we show the number density of stars at  $R \approx 7.45, 8.2$  and  $8.55$  kpc from the Galactic centre. Many

substructures appear in this coordinate space, showing how complex the velocity distribution in the SNd is. The  $v_R$ - $v_\phi$  structure is nearly self-similar in three regions along the radius, with a clear vertical shift of the main features that suggests an approximate conservation of the mean angular momentum of the underlying density structures (see also Ramos et al. 2018).

We briefly describe the most notable features of the local velocity distribution. The Hercules stream indeed consists of two (or even three) features that are horizontally aligned in the SNd, but are slightly tilted in the inner (negative inclination) and outer disk (positive inclination). These several low- $v_\phi$  features are separated from a central blob (near the LSR) by a diagonal gap that gradually decreases its mean azimuthal velocity with larger galactocentric distance. Several features that were previously identified as the Horn, Hyades, Pleiades, and Coma Berenices beyond the gap are superposed. Next, beyond Sirius, there is another sharp break in the density distribution separating a very high-velocity feature, the Hat. Almost all the features can be traced out to  $\approx 0.5$ – $0.8$  kpc from the solar radius, and the groups of stars associated with different SNd moving groups can be also found at different Galactic radii. Although it was thought for a long time that the  $v_R$ - $v_\phi$  moving groups are the local group of stars, the *Gaia* data show their significant radial extent, which has been reported by Ramos et al. (2018), who found that many of the SNd  $v_R$ - $v_\phi$  kinematic substructures can be traced over 2–3 kpc along the radius. This implies that their nature is non-local.

To identify the stars contributing to the different features more precisely, a wavelength analysis has been used (see e.g. Kushniruk et al. 2017; Ramos et al. 2018); however, roughly same results can be obtained by applying unsharp masking (see Eq. (2)) to the density maps presented in Fig. 9 (top). The result is presented in the second row of Fig. 9, where numerous features appear to be more prominent and isolated from each other, especially at the outskirts of the density distribution. To sharpen the features even more, we show only the positive part of the residual maps and highlight the overdensities with different colour boxes (third row). The boundaries of the selections are somewhat arbitrary, but we are confident that the main components are reliably measured because we obtain a similar sample of features as presented in Ramos et al. (2018). However, in our analysis, their A11-A12 features seem to represent a single component.

After the stars are selected in the  $(v_R, v_\phi)$  plane, their angular momenta can be determined. Similar as for the  $(R, v_\phi)$  ridges, we can determine how well they can be associated with the stellar density structures (spiral arms and main bar resonance). In other words, we can determine the locus of the orbits of stars in different  $v_R$ - $v_\phi$  features. The bottom row of Fig. 9 shows the distributions of guiding radii  $R_g$  (or angular momenta) of stars found in different  $v_R$ - $v_\phi$  features. We also marked the location of the MW spiral arms and the bar resonances from Khoperskov et al. (2020a) (corresponding colour bands in Fig. 5 and colour ridges in Fig. 8). First, we note that the  $v_R$ - $v_\phi$  features, being identified at different galactocentric radii, coincide well with each other in the angular momentum space. Second, the agreement between the  $v_R$ - $v_\phi$  features and various in-plane stellar density structures (both spiral arms and main bar resonances) in the angular momentum space implies that the so-called local moving groups are in fact pieces of the large-scale stellar density structures in the MW disk. In particular, the match between these local  $v_R$ - $v_\phi$  features and the MW structures suggests for example that the Arcturus stream is a low-velocity tail of the Scutum-Centaurus spiral arm, part of the Hercules stream corresponds to the bar corotation (see, also, Binney 2020) and its top part

is likely to be the Sagittarius arm, the Sirius stream represents the bar OLR (see also Trick 2022; Binney 2020), and the Hat is likely to be a high-velocity tail of the Perseus arm. We cannot properly associate three tiny  $v_R$ - $v_\phi$  features, but we expect that they are likely to be either high-order resonances of the bar (see, e.g. Monari et al. 2019b; Barros et al. 2020; Asano et al. 2020) or previously unknown weak arms or spurs or featherings of the main MW spiral arms.

### 3.3. Summary of the MW phase-space

In this section, we started the analysis of the density structure and kinematics in the angular momentum space depicting several large-scale azimuthally extended ( $\sim 60^\circ$ ) overdensities. The loci of these overdensities coincide with the MW spiral arms identified by the location of high-mass star-forming regions. This implies that the angular momentum peaks contain the stars of the spiral structure. For the first time, we also demonstrated that in  $(X, Y)$  coordinates, the spiral structure can be directly detected as regions in the disk with a higher fraction of cold-orbit stars (near their guiding centres). Stars in the angular momentum overdensities (spiral arms and the bar resonances) can be traced along the  $(R, v_\phi)$  density ridges. Once these radially extended ridges pass through the SNd region, in the  $v_R$ - $v_\phi$  space the main structures are identified as previously-known moving groups (see also Quillen & Minchev 2005; Quillen et al. 2018). The resonances of the bar show the same behaviour of contributing to the Hercules and Sirius streams for corotation and the OLR, respectively. Therefore we conclude that the most prominent moving groups in the  $v_R$ - $v_\phi$  space are the pieces of the MW spiral arms and the bar resonances. In other words, the so-called local moving groups are not local.

### 3.4. Other interpretations of the $v_R$ - $v_\phi$ plane substructures

Because our analysis of the overdensities in the local  $v_R$ - $v_\phi$  velocity plane is based on the properties of the large-scale angular momentum structures, it is interesting to discuss and compare with alternative interpretations of some of these features. For instance, using the kinematics of the *Gaia* stars in a small annulus around the solar radius, Monari et al. (2019a) argued that the constant angular momentum with azimuth for the second ridge of Hercules is unexpected for the corotation of the bar. However, the more recent determination of corotation for a decelerating bar by Chiba & Schönrich (2021) appears to agree with our prediction of  $v_\phi$ .

Monari et al. (2019b) showed that a locally slightly declining rotation curve would displace the bar resonances at the top of Hercules for the corotation and at the location of the Hat for the OLR. We note here that assuming a slightly incorrect rotation curve in the guiding radius transformation changes the  $R_g$  of the AM overdensities, but because the stars identified with them are back-transferred to  $(X, Y)$  before we compare them with the observed  $v_R$ - $v_\phi$  diagram, this has no influence on their final  $v_\phi$  velocities. Similarly, the assumed value of the solar velocity causes the same shift for the observed stars and the subset of stars identified with an overdensity.

As we discussed above, only the main  $v_R$ - $v_\phi$  features are associated here with the spiral arms and/or major (corotation and OLR) bar resonances. However, we do not rule out scenarios in which some  $v_R$ - $v_\phi$  features may represent high-order resonances of the bar (see e.g. Monari et al. 2019b; Asano et al. 2020). According to some simulations of barred galaxies (see, e.g. Athanassoula 2002; Ceverino & Klypin 2007), the number

of stars trapped by the high-order bar resonances is substantially smaller than the populations of corotation and the OLR. Thus the  $v_R$ - $v_\phi$  features associated with high-order resonances are expected to be significantly weaker (contain fewer stars) than the corotation or OLR streams.

For a long time, dissolved star clusters were thought to cause the main moving groups in the  $v_R$ - $v_\phi$ -space (Eggen 1965; Skuljan et al. 1997; De Silva et al. 2007). Recent models suggest that disrupted star clusters can be detected in the  $v_R$ - $v_\phi$  space no longer than  $\sim 1$  Gyr after their formation (Kamdar et al. 2019), and thus their remnants are unlikely to be prominent over a wide range of galactocentric radii because of the rapid distortion, especially in the presence of the spiral arms.

#### 4. *Gaia* and spectroscopic surveys: Chemical abundances in the SNd, ( $R$ , $v_\phi$ ), ( $X_g$ , $Y_g$ ), and $R_g - z/V_z$

A combination of stellar kinematic and abundance information based on high-resolution spectroscopy is a valuable instrument for exploring the present-day properties and evolution of the MW stellar populations. To study chemical abundance trends associated with the MW spiral arms and bar resonances, we cross-matched the G3RV2 catalogue with Galah DR3, APOGEE DR16 (astroNN), and LAMOST DR5 stars.

We adopted the data from the public version of GALAH DR3 (Buder et al. 2021)<sup>2</sup>, where stellar abundances are derived using the code Spectroscopy Made Easy (Piskunov & Valenti 2017). For our study, we used only stars with a signal-to-noise ratio of  $>20$ , `cannon_flag` = 0, and `abundance_flag` < 3, which result in a precision of the individual abundances of  $\sim 0.05$  dex. We used the data from the high-resolution ( $R \approx 22500$ ) spectroscopic survey APOGEE DR 16 (Majewski et al. 2017; Ahumada et al. 2020), adopting the astroNN catalogue (Leung & Bovy 2019; Bovy et al. 2019)<sup>3</sup>, from which we selected the stars with uncertainties  $< 0.05$  dex in both [Fe/H] and  $[\alpha/\text{Fe}]$ . Finally, we adopted the stellar abundance catalogue of Xiang et al. (2019)<sup>4</sup> derived from the LAMOST DR5 low-resolution spectra ( $R \sim 1800$ , Luo et al. 2015; Xiang et al. 2017), where abundances are measured using the DDPayne (Ting et al. 2019; Xiang et al. 2019). Here we selected only stars with recommended labels and a signal-to-noise ratio of  $>30$  for which the chemical abundances have a typical precision  $\sim 0.05$ – $0.07$  dex.

For each survey, we obtain a cross-matched catalogue of stars with precise [Fe/H] and  $[\alpha/\text{Fe}]$  from the spectroscopic catalogue and positions and velocities from G3RV2, which we refer to as G3RV2+GAL samples for Galah, APOGEE, and LAMOST. For the stars in common between these spectroscopic samples for both [Fe/H] and  $[\alpha/\text{Fe}]$ , we observe clear one-to-one relations, but with some systematic shift and scatter. This is likely due to different spectral resolution and techniques for measuring the stellar parameters, which does not allow us to merge the catalogues easily. In the following sections, we therefore search for chemical abundance features in MW with the three samples separately, taking advantage of the large number of stars in each. For an additional exploration, see also Appendix A.

<sup>2</sup> <https://www.galah-survey.org/dr3/overview/>

<sup>3</sup> <https://data.sdss.org/sas/dr16/apogee/vac>

<sup>4</sup> <http://dr5.lamost.org/doc/vac>

#### 4.1. Chemical abundances in the SNd

Metallicity variations of stars associated with the known  $v_R$ - $v_\phi$  moving groups have been reported in a number of previous studies (see e.g. Bensby et al. 2007, 2014; Williams et al. 2009; Zhao et al. 2014; Kushniruk & Bensby 2019). Broadly speaking, most of the  $v_R$ - $v_\phi$  substructures are not chemically homogeneous. The abundance patterns are almost indistinguishable from those of the background field stars of the Galactic disk (thick or thin; see e.g. Nordström et al. 2004; Bensby & Feltzing 2006; Ramya et al. 2012; Kushniruk & Bensby 2019; Kushniruk et al. 2020). Thus dynamical mechanisms must generally be responsible for the  $v_R$ - $v_\phi$  substructures, such as resonances of the Galactic bar and/or the Milky Way spiral arms (see e.g. Dehnen 2000; Pérez-Villegas et al. 2017b; Monari et al. 2018; Quillen et al. 2018; Barros et al. 2020).

In Fig. 10 we show the density maps together with the mean metallicity distributions in the  $v_R$ - $v_\phi$  plane for SNd stars in common between G3RV2 and the aforementioned surveys. We note that the samples of stars in each cross-match (Galah, AstroNN, LAMOST) with G3RV2 are large enough to represent the  $v_R$ - $v_\phi$  density structure well, which we already discussed in Sect. 3.2 (see Fig. 9), where several of the main kinematic substructures appear to be still rather prominent. Because the contribution of the thick-disk stars is thought to be significant in the SNd region (see Sect. 5.1.3 in Bland-Hawthorn & Gerhard 2016), we focus on the stars with  $[\alpha/\text{Fe}] < 0.1$  to highlight the metallicity composition of the  $v_R$ - $v_\phi$  phase-space. This cut does not fully guarantee a clean thin-disk stars sample, but it significantly reduces a contamination from the chemically defined thick disk, which is likely to have a different formation history (see e.g. Haywood et al. 2013) and thus different kinematic properties (see e.g. Lee et al. 2011).

Figure 10 first shows a monotonic decrease in mean metallicity with increasing azimuthal velocity. Because in the local SNd, azimuthal velocity is a proxy of the guiding radius (or angular momentum), this metallicity trend represents the negative radial metallicity gradient in the MW thin disk along the guiding radius (see e.g. Katz et al. 2021). Following an inside-out galaxy formation scenario (e.g., Chiappini et al. 1997), stars that formed in the inner galaxy have higher metallicities, but also larger radial excursions (or asymmetric drift) in the SNd. This means that they mainly contribute in the lower part of the  $v_R$ - $v_\phi$  plane (third row in Fig. 10). On the other hand, stars that formed in the outer disk, beyond the solar radius, have lower metallicities on average, but they can still be found in the SNd at azimuthal velocities higher than the LSR value (third row in Fig. 10).

In the mean metallicity maps in Fig. 10, a very sharp, curved decrease in the mean metallicity above  $v_\phi \approx 20 \text{ km s}^{-1}$  is visible. This prominent gradient implies that there is a mechanism that limits the outward motion of the high-[Fe/H] stars beyond  $R_g \approx 9$ – $10$  kpc. The most natural explanation is the presence of the OLR of the bar, which does not allow the stars to pass through and thus is a natural barrier between the inner  $< 9$ – $10$  kpc and the outer disk (Haywood et al. 2019). This has been suggested in a number of studies of barred galaxy dynamics (Halle et al. 2015; Khoperskov et al. 2020b; Wozniak 2020). It is worth mentioning that the orbits of stars can temporally cross the bar OLR (see Monari et al. 2016b), but the stars cannot change their angular momentum to pass through the OLR from the inner galaxy. The azimuthal velocity ( $\propto$  guiding radius in the SNd) of the OLR-caused metallicity

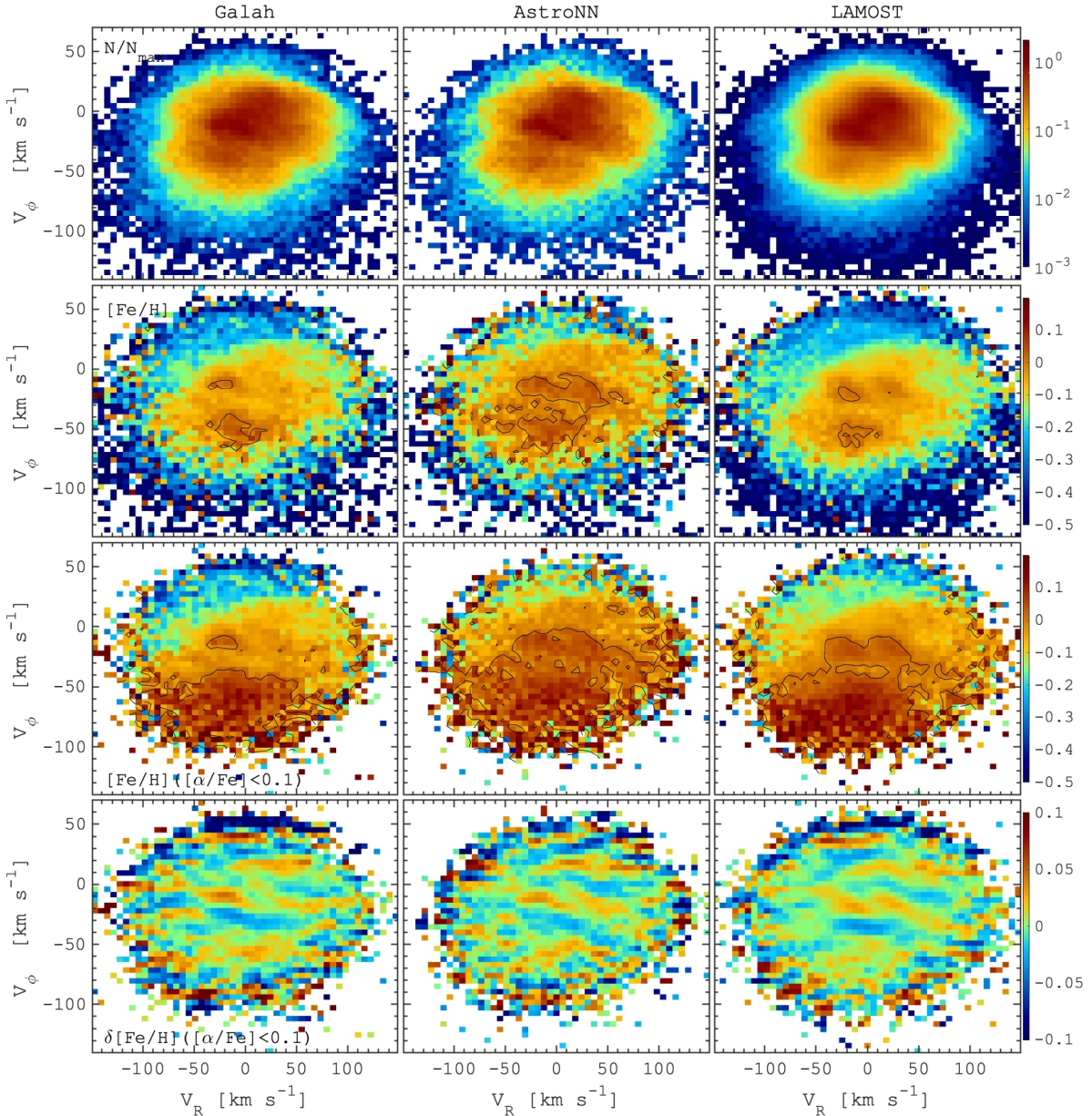


**Fig. 10.** Kinematic  $v_R$ - $v_\phi$  space for the G3RV2 stars in the SND cross-matched with Galah (*left*), AstroNN (*centre*), and LAMOST (*right*). Density distribution (*first row*), colour-coded by the mean  $[\text{Fe}/\text{H}]$  (*second row*), the mean  $[\text{Fe}/\text{H}]$  for thin-disk stars (low- $\alpha$  sequence, *third row*), and the residual  $[\text{Fe}/\text{H}]$  distribution for low- $\alpha$  stars (*bottom row*). The  $v_R$ - $v_\phi$  features are well established with the higher mean metallicity ( $\delta[\text{Fe}/\text{H}] \approx 0.05$  dex), and two groups of kinematic features are separated by low- $[\text{Fe}/\text{H}]$  gaps behind the corotation (Hercules streams) and the OLR (Sirius stream). At a given galactocentric radius, the metallicity gradient as a function of the azimuthal velocity reflects the metallicity gradient in the MW along the guiding radius (or angular momentum).

pattern we observe corresponds to the most recent direct estimates of its pattern speed of  $\approx 38$ – $41 \text{ km s}^{-1} \text{ kpc}^{-1}$  (Clarke et al. 2019; Sanders et al. 2019; Bovy et al. 2019). Another argument in favour of the OLR-impact on the SND metallicity distribution is based on the distribution function calculations by Binney (2020), where the MW bar OLR is placed in the same region we suggest here (beyond the Sirius stream). This also agrees with our previous estimates of the locations of the large-scale structures based on the guiding space analysis (Khoperskov et al. 2020a). When the OLR location is constrained in the  $v_R$ - $v_\phi$  space, the bar corotation radius should be placed near the Hercules stream(s) (which corresponds to  $R \approx 6 \text{ kpc}$  from the Galactic centre), thus also supporting a number of

recent studies (Pérez-Villegas et al. 2017b; Monari et al. 2019a; D’Onghia & Aguerrí 2020; Asano et al. 2020).

Next we discuss the metallicity features focusing on the moving groups in the  $v_R$ - $v_\phi$  space. In Fig. 10 most of the kinematic substructures are visible as groups of stars that tend to have a slightly higher metallicity than the local mean value. The typical difference of the  $v_R$ - $v_\phi$ -plane features in the median metallicity is 0.05 dex, which is somewhat similar to the numbers found by Antoja et al. (2017) based on RAVE data. As we discussed above, the local moving groups are the pieces of the MW spiral arms and the bar resonances. Therefore the enhancement of the metallicity in the  $v_R$ - $v_\phi$  space should correspond to an enhancement characterising the spiral arms on larger spatial scales. We

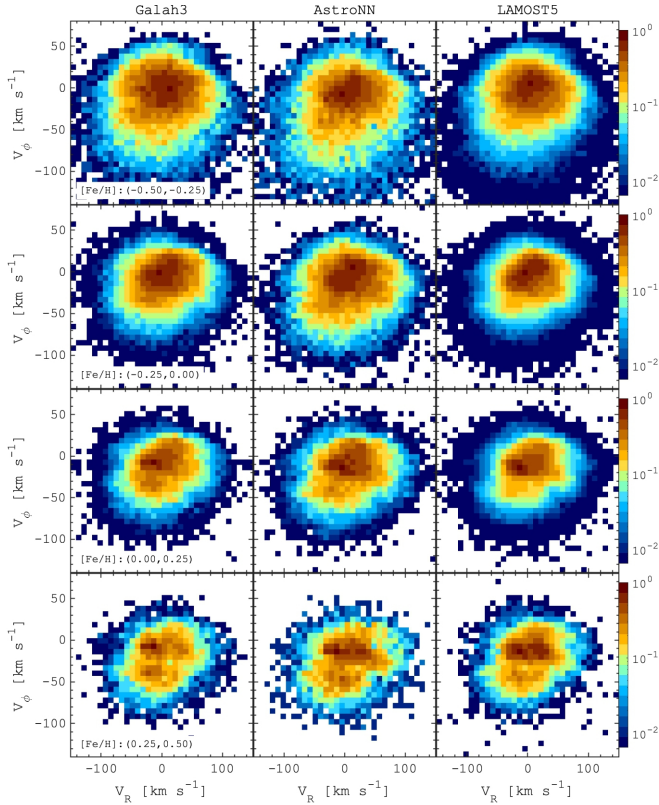


**Fig. 11.** Number density of stars in different metallicity bins in the  $v_R$ - $v_\phi$ -coordinates for the G3RV2 sample cross-matched with Galah (*left*), AstroNN (*centre*) and LAMOST (*right*).

return to this problem below after we present the metallicity distributions in other phase-space coordinates (see Sect. 4.5).

Figure 11 shows the density distributions in the  $v_R$ - $v_\phi$  plane in several  $[\text{Fe}/\text{H}]$  bins. The variation in the distribution shape depicts the correlation between the stellar metallicity and the spread of the radial and azimuthal velocity components (velocity dispersion). In particular, the distribution is broader for low- $[\text{Fe}/\text{H}]$  stars, while high- $[\text{Fe}/\text{H}]$  stars tend to have lower peculiar velocities. Very high- $[\text{Fe}/\text{H}]$  stars ( $>0.25$ ) show prominent overdensities in the area corresponding to the Hercules, Pleiades, Hyades, and the Horn, with a very sharp decrease in density above the Sirius stream. At the same time, the lowest- $[\text{Fe}/\text{H}]$  distribution, which is blurred, still shows an asymmetric distribution reflecting the presence of the Hercules stream and a weak signal for Pleiades, Hyades, and Horn stars in this metallicity range. This picture suggests that the most prominent ( $v_R$ - $v_\phi$ ) overdensities show a wide range in metallicity (from  $-0.5$  to  $+0.5$ ), which implies that they are chemically homogeneous. An exception here are the  $v_R$ - $v_\phi$  streams with their very high  $v_\phi$  velocity, which is higher than the LSR (the Hat). This feature demonstrates a lack of high-metallicity stars ( $[\text{Fe}/\text{H}] > 0.25$ ) because these phase-space features are likely caused by the stellar density structures in the low- $[\text{Fe}/\text{H}]$  outer disk beyond the OLR of the bar (Sirius stream).

We take another example from the opposite side of the  $v_R$ - $v_\phi$  plane. For a long time, the Arcturus stream ( $v_\phi \sim -100 \text{ km s}^{-1}$ ) has been associated with a relic of a disrupted extragalactic object (Navarro et al. 2004; Helmi et al. 2006). Although the density distributions in Fig. 11 do not reveal the Arcturus stream as an overdensity (but see Fig. 9 for the *Gaia* stars), we can note the presence of high- $[\text{Fe}/\text{H}]$

stars ( $0-0.25$  dex) near  $v_\phi \sim -100 \text{ km s}^{-1}$ , which indicates that the group of stars is likely to be a part of the stellar density structure in the inner disk of the MW (including thick disk stars Williams et al. 2009; Helmi et al. 2014; Antoja et al. 2015), which according to our previous analysis (see Fig. 9), is associated with the innermost spiral arm (Scutum-Centaurus), and its extragalactic origin can be ruled out. The presence of stars in a wide range of  $[\text{Fe}/\text{H}]$  near the Arcturus stream probably agrees with more detailed chemical abundance studies (Ramírez & Allende Prieto 2011; Ramya et al. 2012; Bensby et al. 2014), suggesting that the dynamical origin of the Arcturus stream consists of a mixture of thin- and thick-disk stars that formed at different galactic radii.

#### 4.2. Chemical abundance patterns in the $(R, v_\phi)$ coordinates

Chemical abundance patterns associated with diagonal  $R$ - $v_\phi$ -ridges have been presented in a number of studies (Khanna et al. 2019; Liang et al. 2019; Wheeler et al. 2020; Wang et al. 2020a,b). For instance, Khanna et al. (2019) suggested that the ridges are metal-rich because they are made of younger stars that lie predominantly in the plane. Numerical simulations also demonstrate that, for instance, the OLR-related  $(R, v_\phi)$  ridges contain younger, metal-rich, and  $\alpha$ -poor stars compared to the surrounding regions, suggesting that this might be caused by the fact that colder populations are more affected by the resonances caused by the bar (Fragkoudi et al. 2020). Alternatively, this chemical abundance behaviour near the bar resonances can be explained by the outward migration of stars that are trapped at the bar resonances due to the slow-down of the bar over time (see more details in Khoperskov et al. 2020b). In this case, the stellar age distribution in the CR and OLR ridges can be used to constrain the age of the bar and the epoch of its slow-down.

In Fig. 12, similar to the previous figure of  $v_R$ - $v_\phi$  coordinates, we present the density and mean metallicity maps in the  $(R, v_\phi)$  plane for stars around  $10^\circ$  along the line connecting the Galactic centre and the Sun. First, we note a sharp decrease in metallicity above the ridge, which we associated with the bar OLR. It is clearly visible in  $v_R$ - $v_\phi$  space above the Sirius stream. Because the motions of thick disk stars are less affected by the structures in the Galactic plane, we again suggest that the  $[\text{Fe}/\text{H}]$  patterns of the ridges are more prominent when we remove stars of the thick disk (high- $\alpha$ ). In Fig. 12 (third row) we show the mean metallicity maps for the low- $\alpha$  (or chemically defined thin-disk) stars. A large-scale diagonal shape of the metallicity gradient is obviously caused by the contribution of inner, metal-rich stars at larger radial excursion to lower  $v_\phi$  regions at large galactocentric radii. Interestingly, the tilt of the mean metallicity distribution implies that the metallicity gradient is more tightly connected to the angular momentum than to galactocentric distance (Katz et al. 2021). When the  $[\text{Fe}/\text{H}]$  gradient (bottom row of Fig. 12) is extracted, the density ridges appear to show a higher metallicity with an amplitude of 0.05 dex. This confirms that the  $v_R$ - $v_\phi$  metallicity features are the patches of large-scale structures spanning over the entire MW disk.

#### 4.3. Chemical abundance patterns in the $(X_g, Y_g)$ coordinates

In Fig. 13 we present two-dimensional metallicity variations in the Galactic plane in  $(X_g, Y_g)$  guiding coordinates. Similar to the previous figures of this section, we show the mean maps of stellar density,  $[\text{Fe}/\text{H}]$ ,  $[\alpha/\text{Fe}]$  ( $[\alpha/\text{Fe}] < 0.1$ ), and  $\delta[\text{Fe}/\text{H}]$  for the Galah, APOGEE, and LAMOST surveys cross-matched with

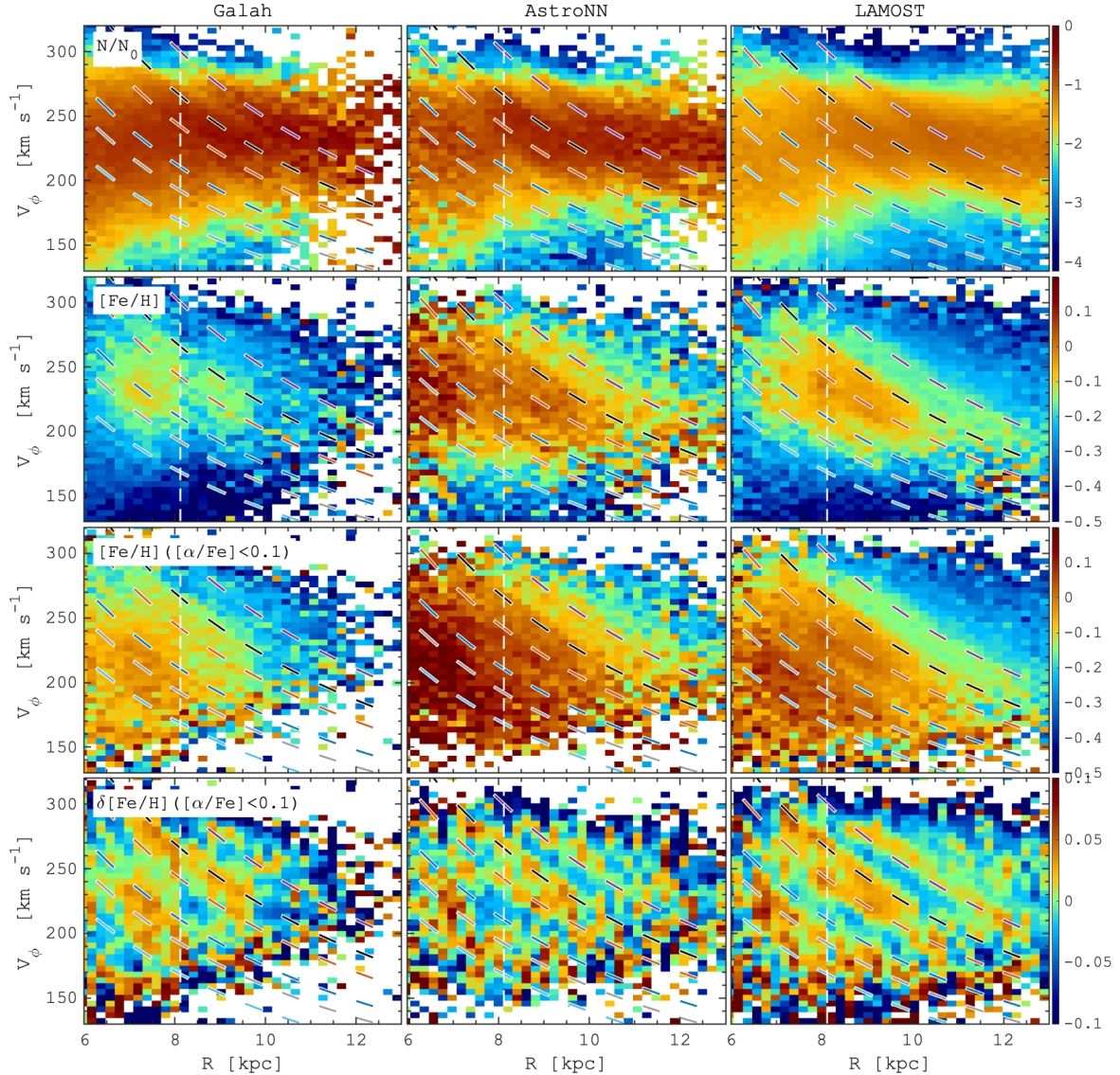


**Fig. 12.** Similar to Fig. 10, but in  $(R, v_\phi)$  space for the G3RV2 stars cross-matched with Galah (*left*), AstroNN (*centre*), and LAMOST (*right*). Density distribution (*first row*), colour-coded by the mean  $[\text{Fe}/\text{H}]$  (*second row*), the mean  $[\text{Fe}/\text{H}]$  for thin-disk stars (low- $\alpha$  sequence, *third row*), and the residual  $[\text{Fe}/\text{H}]$  distribution for low- $\alpha$  stars (*bottom row*). The coloured diagonal lines are the same as in Fig. 8 and depict the angular momentum selections in a given azimuthal range used in  $(X_g, Y_g)$  coordinates to identify overdensities in Khoperskov et al. (2020a) (see also Fig. 5). The  $(R, v_\phi)$  density ridges are well-established structures with the higher mean metallicity ( $\delta[\text{Fe}/\text{H}] \approx 0.05$  dex). The impact of the OLR is seen as a sharp decrease in metallicity beyond the black line.

G3RV2 separately. The density maps have different coverage in  $(X_g, Y_g)$  plane because of the different survey footprints. However, all the data sets are large enough and show the existence of trailing angular momentum overdensities, which, as we showed above, correspond to the MW spirals and the bar resonances (see Fig. 5 and Khoperskov et al. 2020a). The mean  $[\text{Fe}/\text{H}]$  maps reveal a tight relation between these overdensities with narrow regions of enhanced (relative amplitude  $\delta[\text{Fe}/\text{H}] \approx 0.05$ ) metallicity. Similar to Fig. 10 and 12, we found a large-scale sharp decrease in mean metallicity beyond the overdensity associated with the bar OLR, which is even more prominent for the low- $\alpha$  stars. The most exciting result here are the azimuthally extended metallicity-enhanced structures: spiral arms that imply that the chemical abundance peculiarities we discussed above is a large-scale phenomenon that can only be caused by global mechanisms that reshape stellar populations across the entire MW disk.

#### 4.4. Chemical abundance patterns across the disk plane in $R_g - z$ and $R_g - v_z$ coordinates

The last piece of our analysis involves the exploration of chemo-kinematic features perpendicular to the Galactic plane. Various velocity patterns perpendicular to the Galactic plane have been intensively discussed in a number of previous observational studies, implying the importance of various factors (see e.g. Williams et al. 2013; Widrow et al. 2014; Gaia Collaboration 2018a; Carrillo et al. 2019), including the impact of the spiral arms (Faure et al. 2014; Monari et al. 2016a). To link our previous analysis with the vertical manifestation of spirals in Fig. 14, we present the radial velocity and metallicity maps in  $R_g - z$  (left) and  $R_g - v_z$  (right) coordinates for the stars taken in a narrow azimuthal selection (same as for the  $(R, v_\phi)$  analysis).

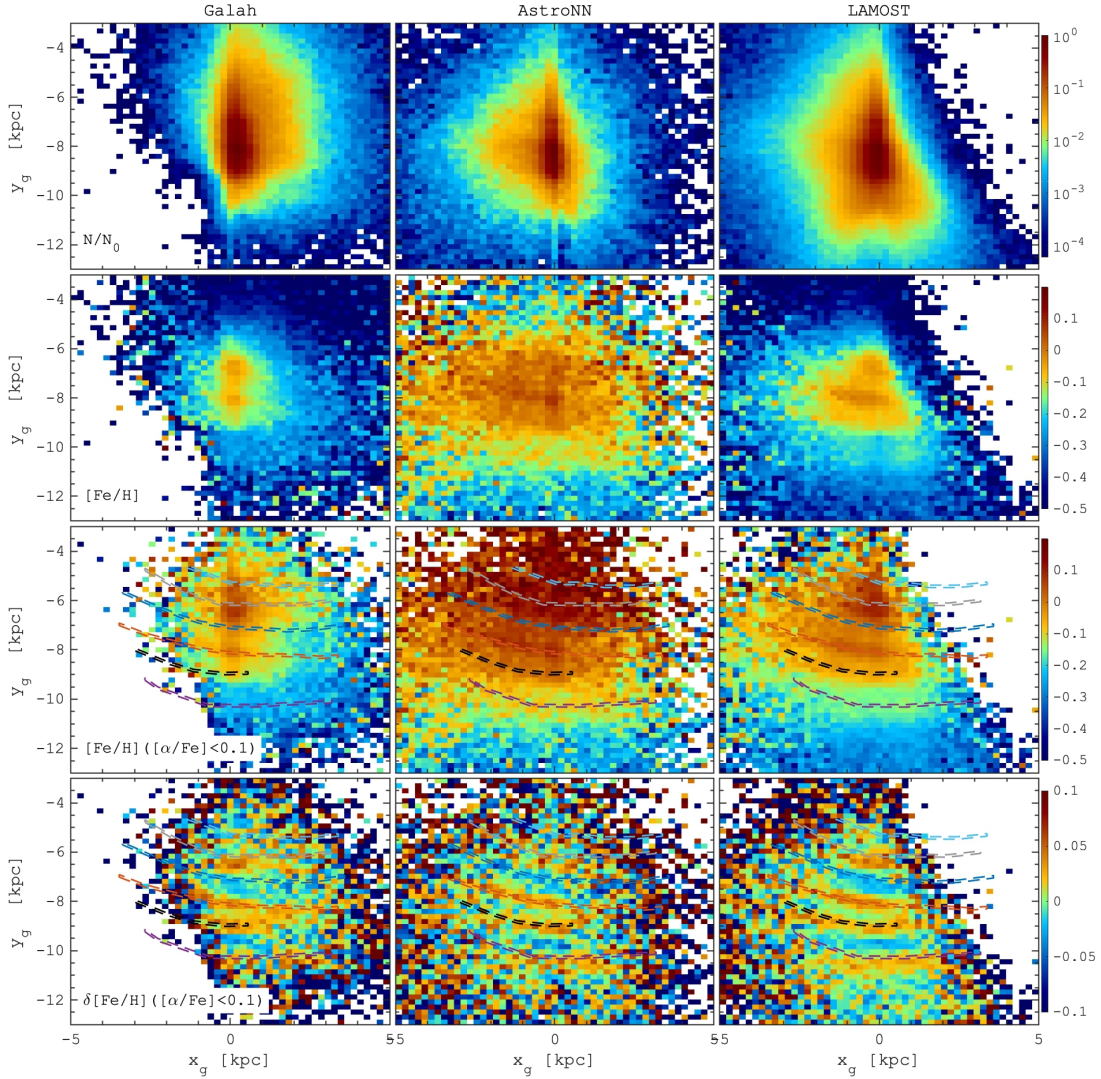


**Fig. 13.** Similar to Figs. 10 and 12, but in angular momentum ( $X_g, Y_g$ ) space for the G3RV2 stars cross-matched with Galah (left), AstroNN (centre), and LAMOST (right). Density distribution (first row), colour-coded by the mean  $[\text{Fe}/\text{H}]$  (second row), the mean  $[\text{Fe}/\text{H}]$  for thin-disk stars (low- $\alpha$  sequence, third row), and the residual  $[\text{Fe}/\text{H}]$  distribution for low- $\alpha$  stars (bottom row). The locations of tightly wound trailing regions of the higher mean metallicity ( $\delta[\text{Fe}/\text{H}] \approx 0.05$  dex) correlate with the stellar overdensities associated with the main MW spiral arms.

Figure 14 shows prominent wave-like radial velocity waves along  $R_g$ , as we already described in Fig. 5, where the negative radial motions roughly correspond to the location of the spiral arms (see also Siebert et al. 2012; Faure et al. 2014; Antoja et al. 2016). The striking feature of this pattern is its vertical extension. In particular, G3RV2 stars show the wave-like pattern out to  $z \approx 2$  kpc and  $v_z \approx 75$  km s<sup>-1</sup>. These numbers are slightly lower for the G3RV2+GAL stars likely due to lower statistics. The vertical extension of the radial velocity pattern suggests that the spiral arms contain relatively (dynamically) old stars with a significant vertical excursion because they, which were formed in a thin gaseous disk, already experienced some vertical heating. Therefore, the data suggest that the spiral arms of the MW cannot be interpreted as a newly formed structure that is visible only among young stars.

The vertical structure of the mean  $[\text{Fe}/\text{H}]$  distribution shows a less prominent wave-like pattern than the radial velocity maps. However, when we removed the background distribution (radial gradient), the residual distributions showed noticeable  $[\text{Fe}/\text{H}]$  variations following the radial velocity pattern. The enhancement of the mean metallicity is close to the negative radial

velocity regions and is therefore associated with the spiral arms, similar to our analysis of  $(R, v_\phi)$  and  $v_R-v_\phi$  planes in previous sections. The amplitude of the metallicity variations is in the range of 0.05 dex as in other phase-space coordinates. These variations can be traced up to  $0.8 - 1$  kpc, which is slightly lower than those for the radial velocity, but this is likely the result of lower statistics and relatively large chemical abundance errors compared to the amplitude of the systematic  $[\text{Fe}/\text{H}]$  pattern. Therefore, these results rule out the scenario proposed by Khanna et al. (2019) to explain the  $(R, v_\phi)$  ridges by young stars alone because the main  $(R, v_\phi)$  ridges correspond to the spiral arms, which can be traced far away from the Galactic plane.

#### 4.5. Mechanism of the $[\text{Fe}/\text{H}]$ pattern formation in the vicinity of spiral arms

To summarise the results of this section, our analysis of the chemical abundance distribution demonstrates the existence of multiple large-scale stellar density structures with a metallicity that is higher by 0.05 dex. These  $[\text{Fe}/\text{H}]$  patterns follow the spiral arms that were derived as angular momentum

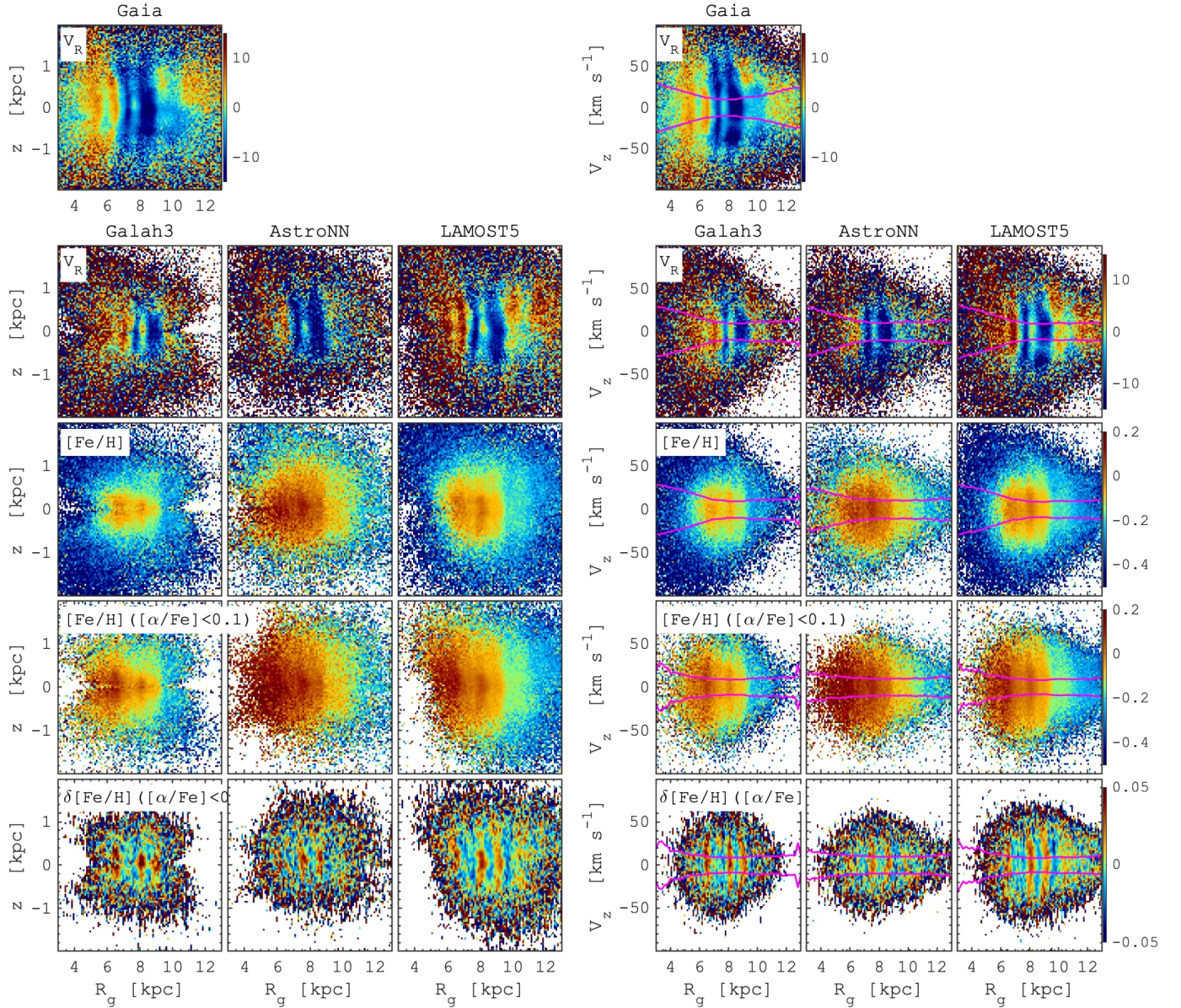


**Fig. 14.** Radial velocity and metallicity maps in  $R_g - z$  (left) and  $R_g - v_z$  (right) coordinates taken in a narrow  $\pm 5^\circ$  azimuthal selection centred on the Sun-Galactic centre line. The magenta contours in the *right panels* show  $1\sigma$  levels of the vertical velocity distribution. *Top panels:* mean radial velocity maps for the G3RV2. The following rows represent the mean radial velocity, the mean  $[\text{Fe}/\text{H}]$ , the mean  $[\text{Fe}/\text{H}]$  for  $[\alpha/\text{Fe}] < 0.1$ , and the residual (relative to the extracted 2D gradient)  $[\text{Fe}/\text{H}]$  maps for the G3RV2 stars in common with Galah (*left*), AstoNN (*centre*), and LAMOST (*right*). The radial velocity wave-like pattern, correlating with the stellar overdensities in  $(X_g, Y_g)$  and  $(R, v_\phi)$  coordinates (see Figs. 5 and 8), shows a large vertical extension. This suggests that the spiral arms and bar resonances can be traced far from the Galactic plane by stars with high vertical velocities. Similarly, the  $[\text{Fe}/\text{H}]$  pattern is detected significantly away from the Galactic plane, consistent with the radial velocity variations.

overdensities that are traceable in the azimuthal direction across the entire G3RV2 footprint, in the radial direction in the form of the  $(R, v_\phi)$  ridges, as local  $v_R - v_\phi$  moving groups in the SND, and finally, up to 0.8–1 kpc away from the Galactic plane. Several different mechanisms can be involved in order to explain the origin of the chemical abundance patterns presented in Figs. 10–14, such as (i) radial migration, (ii) a local enrichment, and (iii) kinematic fractionation<sup>5</sup>.

(i) In the presence of a radial metallicity gradient, stellar radial migration results in the azimuthal variation in the resid-

ual metallicity characterised by a metal-rich trailing edge and a metal-poor leading edge of the spirals (Grand et al. 2016). In this case, the  $[\text{Fe}/\text{H}]$  pattern we discover would be the perfect manifestation of ongoing radial migration in the MW. However, the radial migration is most effective for stars on nearly circular orbits in the vicinity of the corotation (Sellwood & Binney 2002), which for the slowly rotating MW spiral arms (see Bland-Hawthorn & Gerhard 2016 for the review) is located beyond the solar radius. Therefore, ongoing stellar migration cannot be responsible for the observed patterns in the inner disk. Some  $N$ -body models suggest that rather open (large pitch angles) spiral arms could be corotating structures where the corotation is located everywhere along the arms (see e.g.

<sup>5</sup> Originally proposed for the stellar populations separation in the presence of a bar in Debattista et al. (2017).

Grand et al. 2015). However, the MW spiral arms are usually assumed to be rigidly rotating with a certain pattern speed, and there is no direct evidence yet in favour of the corotating nature of the MW spirals. Finally, there are no theoretical predictions concerning the vertical abundance patterns near the spirals that are caused by the radial migration.

(ii) Another process that might be responsible for the metallicity enhancement in spirals is discussed by Spitoni et al. (2019), where 2D chemical evolution models predict a local ISM enrichment leading to a faster chemical evolution (and thus higher metallicity of stars) near the corotation radius. To explain a higher metallicity of the spirals in the MW, we again need to assume a corotating nature of the spirals in this case, which should resemble their structure for a long time (enough to increase the metallicity of the ISM locally). This contradicts the  $N$ -body simulations, however, in which spiral arms rapidly change the structure.

(iii) Finally, it is worth mentioning a mechanism that is independent of the nature of spiral arms, implying an enhancement of the mean metallicity near the spirals in the presence of multiple populations with different chemo-kinematical properties. In particular, assuming a decrease in stellar velocity dispersion with metallicity (assuming a realistic age-metallicity and age-velocity dispersion relations), it has been shown that a differential kinematical response of these stellar populations on the spiral arm gravitational potential leads to the azimuthal variations of the mean metallicity across the spiral arms (Khoperskov et al. 2018b).

The understanding of mechanisms driving the observed metallicity pattern in the vicinity of the spiral arms is yet beyond the scope of our work. More detailed chemical and dynamical models of MW-type spiral galaxies are needed.

## 5. Summary and conclusions

We first studied a new high-resolution  $N$ -body simulation of an MW-like disk galaxy during the growth phase of a multi-arm, tightly wound spiral pattern, with the goal of investigating the phase-space structure that this pattern imprints on the stellar disk of the model. By shifting stars to their angular momentum-equivalent guiding radii  $R_g$ , much of the epicyclic blurring is removed, and a sharper view of the galaxy substructure can be obtained (see also Khoperskov et al. 2020a) that is morphologically similar, but not identical to the substructure in the density map (Figs. 1 and 3). We showed that in this simulation, the spiral structure can be recovered by analysing the disk stars in the angular momentum space. In the analysed snapshot, we demonstrated the following:

- The spiral arms have amplitudes 10–15%. They are traced by stars located near the azimuthally extended overdensities in guiding (angular momentum) space (see Fig. 3), in particular, by dynamically cold stars with small  $R - R_g$ .
- The guiding space overdensities allowed us to identify the peak densities of the real-space spiral arms and also contain a fraction of stars that travel far into the disk, leading to phase-space overdensities in disk regions some kiloparsec away from the spiral arm with the same angular momentum.
- In a region of a few kiloparsec and an angular extent of few dozen degrees such as the region surveyed by DR3V2, these overdensities appear as a more nearly vertically extended (along the azimuth) wave-like pattern in the  $(\phi, L_z)$  plane (Fig. 2).

- In the  $(R, v_\phi)$  plane, these angular momentum overdensities give rise to radially extended (3–5 kpc) diagonal ridges with outwardly decreasing  $v_\phi$  (Fig. 4).
- At a typical SNd-like region, the ridges are visible as moving group-like overdensities in local velocity space with similar 10–15% amplitudes (Fig. 4).

In this simulation with a tightly wound multi-arm spiral structure, the main angular momentum overdensities correspond to individual spiral arms. However, this seems not to be universal (Hunt et al. 2020); depending on the model and the nature of the spiral structure (long-lived, transient, tidally induced, grand design, etc.), we may expect that a single spiral may correspond to several angular momentum overdensities.

We chose this simulation because the patterns we observe in the  $N$ -body model are in many respects similar to the phase-space structure observed in the nearby Galactic disk by *Gaia*. Therefore, we applied similar approaches to the Milky Way data. In our analysis of *Gaia* (DR2+EDR3) we find that

- the angular momentum overdensities in DR3V2 data are seen independently within and outside 1 kpc from the Sun, just as in the homogenised *Gaia* data subset in our earlier study (Khoperskov et al. 2020a). They are large-scale, not local features in the surveyed Galactic disk region (Fig. 5).
- most of the *Gaia* stars in the angular momentum overdensities are found close to their guiding radii (e.g.,  $\approx 50\%$  within  $|R - R_g| < 0.4$  kpc, and 95% within 2 kpc, see Fig. 6). For several angular momentum overdensities, the stars within 250 pc of their guiding radii are found in the Galactic plane in locations coinciding with the high-mass star formation regions from Reid et al. (2019), that is, the Sagittarius, Local, and Perseus spiral arms (see Fig. 7). Just as in the  $N$ -body model, spiral overdensities can be identified as overdensities in the dynamically cold stars. The match does not work for the Scutum-Centaurus arm near the end of the bar.
- stars in the angular momentum overdensities follow the known  $(R, v_\phi)$  density ridges. When these radially extended ridges pass through the SNd region, they result in  $v_R - v_\phi$  velocity plane overdensities that match the well-known main moving groups (see Fig. 8 and 9). In this interpretation, from low to high  $V_\phi$ , the Arcturus stream overlaps with low-velocity stars from the Scutum-Centaurus arm overdensity, part of Hercules corresponds to bar corotation, the top part overlaps with the Sagittarius arm overdensity, the Sirius stream lies on the bar OLR, and the high-velocity Hat on the Perseus arm overdensity (see Figs. 9 and Khoperskov et al. 2020a for the bar resonances).

The overlap of the local kinematic features with the main spiral arm angular momentum overdensities suggests their genetic connection, but alternative explanations cannot be ruled out, especially for weaker  $v_R - v_\phi$  features that cannot yet be associated with spirals and may represent higher-order bar resonances (Monari et al. 2019b).

Using additional data from the Galah, APOGEE, and LAMOST surveys, we finally analysed the trends of mean metallicity across these structures.

- Using low- $\alpha$  stars, we find a uniform metallicity gradient in the  $v_R - v_\phi$  plane from low to high  $v_\phi$ , and a corresponding gradient across the  $(R, v_\phi)$  plane and in guiding space, reflecting the outward Galactic gradient (Fig. 10). The supersolar metallicity stars born in the inner disk contribute more strongly at low  $v_\phi$ , while metal-poorer stars dominate at high  $v_\phi$ .
- We find a sharp, curved decrease in the mean metallicity beyond  $R_g = 9$ –10 kpc, which is naturally interpreted as the

bar OLR barrier to the outer disk, as suggested by [Halle et al. \(2015\)](#), [Khoperskov et al. \(2020b\)](#) (see Figs. 10, 12, and 13). Although this OLR feature seems to be rather prominent, the impact of other high-order bar resonances on the chemical abundance variations in the disk is not fully explored in the literature. Using  $N$ -body models, [Wheeler et al. \(2021\)](#) recently predicted a weak  $[\text{Fe}/\text{H}]$  signature of the main 4 : 1 resonance, whose manifestation in the MW requires further investigation.

- Stars of the main moving groups are seen to have a slightly but systematically enhanced mean metallicity (by  $\approx 0.05$  dex) relative to the nearby average value (Fig. 10); this is also visible in the guiding (angular momentum) space overdensities and  $(R, v_\phi)$  ridges (Figs. 12, 13).
- We finally find noticeable periodic  $[\text{Fe}/\text{H}]$  variations as a function of the angular momentum that can be traced up to  $|z| \approx 0.8\text{--}1$  kpc and  $|v_z| \approx 50$  km s $^{-1}$  (Fig. 14). This suggests that the angular momentum overdensities also include stars that experienced substantial dynamical heating.

The enhancement of the metallicity near  $v_R\text{--}v_\phi$  features and  $(R, v_\phi)$  ridges provides additional arguments in favour of the link between the guiding space overdensities and the MW spiral arms, because these enhancements were predicted in a number of previous chemodynamical models (see Sect. 4.5). In conclusion, these results consistently point to the interpretation that the most prominent phase-space features seen in the *Gaia* data in SNd  $v_R\text{--}v_\phi$  space, the  $(R, v_\phi)$  plane, and the angular momentum diagram are linked to the large-scale MW spiral arms and main bar resonances. Future *Gaia* data releases will have increased spatial coverage of the MW disk, making it possible to map the angular momentum structures at larger distances from the Sun and further test this interpretation. The physical parameters of the stars in the overdensities obtained by future spectroscopic surveys (4MOST, WEAVE, and MOONS) will allow us to better constrain the mechanisms for the discovered metallicity enhancements and in this way shed light on the true nature of the spiral structure in the MW.

*Acknowledgements.* The authors thank the anonymous referee for a constructive report. They also wish to thank Jason Hunt for stimulating this work. SK thanks Dmitrii Byziaev, Jonny Clarke and Shola Wylie for their assistance with access to the APOGEE data; Evgeny Polyachenko for the help with the initial condition generation for the  $N$ -body model; Paola Di Matteo for the access to data storage facilities of the GEPI (Paris Observatory); David Katz and Misha Haywood for several suggestions about the *Gaia* and APOGEE data treatment respectively. SK also thanks Ivan Minchev for several helpful comments on earlier versions of the manuscript. SK acknowledges the Russian Science Foundation (RSCF) grant 19-72-20089 for support in the analysis of the spectroscopic data and the preparation of the  $N$ -body model carried by using the equipment of the shared research facilities of HPC computing resources at Lomonosov Moscow State University (project RFMEFI62117X0011). This work has made use of data from the European Space Agency (ESA) mission *Gaia* (<https://www.cosmos.esa.int/gaia>), processed by the *Gaia* Data Processing and Analysis Consortium (DPAC, <https://www.cosmos.esa.int/web/gaia/dpac/consortium>). Funding for the DPAC has been provided by national institutions, in particular the institutions participating in the *Gaia* Multilateral Agreement. Funding for the Sloan Digital Sky Survey IV has been provided by the Alfred P. Sloan Foundation, the U.S. Department of Energy Office of Science, and the Participating Institutions. Guoshoujing Telescope (the Large Sky Area Multi-Object Fiber Spectroscopic Telescope LAMOST) is a National Major Scientific Project built by the Chinese Academy of Sciences. Funding for the project has been provided by the National Development and Reform Commission. LAMOST is operated and managed by the National Astronomical Observatories, Chinese Academy of Sciences. Software: IPython ([Perez & Granger 2007](#)), Astropy ([Astropy Collaboration 2018](#)), NumPy ([van der Walt et al. 2011](#)), SciPy ([Virtanen et al. 2020](#)), AGAMA ([Vasiliev 2019](#)), Matplotlib ([Hunter 2007](#)), Pandas ([McKinney et al. 2010](#)), TOPCAT ([Taylor 2005](#)).

## References

- Ahumada, R., Prieto, C. A., Almeida, A., et al. 2020, *ApJS*, 249, 3
- Antoja, T., Figueras, F., Fernández, D., & Torra, J. 2008, *A&A*, 490, 135
- Antoja, T., Valenzuela, O., Pichardo, B., et al. 2009, *ApJ*, 700, L78
- Antoja, T., Figueras, F., Romero-Gómez, M., et al. 2011, *MNRAS*, 418, 1423
- Antoja, T., Helmi, A., Dehnen, W., et al. 2014, *A&A*, 563, A60
- Antoja, T., Monari, G., Helmi, A., et al. 2015, *ApJ*, 800, L32
- Antoja, T., Roca-Fàbrega, S., de Bruijne, J., & Prusti, T. 2016, *A&A*, 589, A13
- Antoja, T., Kordopatis, G., Helmi, A., et al. 2017, *A&A*, 601, A59
- Antoja, T., Helmi, A., Romero-Gómez, M., et al. 2018, *Nature*, 561, 360
- Arifanto, M. I., & Fuchs, B. 2006, *A&A*, 449, 533
- Asano, T., Fujii, M. S., Baba, J., et al. 2020, *MNRAS*, 499, 2416
- Astropy Collaboration (Robitaille, T. P., et al.) 2013, *A&A*, 558, A33
- Astropy Collaboration (Price-Whelan, A. M., et al.) 2018, *AJ*, 156, 123
- Athanassoula, E. 2002, *ApJ*, 569, L83
- Barros, D. A., Pérez-Villegas, A., Lépine, J. R. D., Michtchenko, T. A., & Vieira, R. S. S. 2020, *ApJ*, 888, 75
- Belokurov, V., Erkal, D., Evans, N. W., Koposov, S. E., & Deason, A. J. 2018, *MNRAS*, 478, 611
- Belokurov, V., Sanders, J. L., Fattahi, A., et al. 2020, *MNRAS*, 494, 3880
- Bensby, T., & Feltzing, S. 2006, *MNRAS*, 367, 1181
- Bensby, T., Oey, M. S., Feltzing, S., & Gustafsson, B. 2007, *ApJ*, 655, L89
- Bensby, T., Feltzing, S., & Oey, M. S. 2014, *A&A*, 562, A71
- Binney, J. 2020, *MNRAS*, 495, 895
- Bland-Hawthorn, J., & Gerhard, O. 2016, *ARA&A*, 54, 529
- Bland-Hawthorn, J., & Tepper-García, T. 2021, *MNRAS*, 504, 3168
- Bland-Hawthorn, J., Sharma, S., Tepper-García, T., et al. 2019, *MNRAS*, 486, 1167
- Bovy, J., Leung, H. W., Hunt, J. A. S., et al. 2019, *MNRAS*, 490, 4740
- Buder, S., Sharma, S., Kos, J., et al. 2021, *MNRAS*, 506, 150
- Carrillo, I., Minchev, I., Steinmetz, M., et al. 2019, *MNRAS*, 490, 797
- Ceverino, D., & Klypin, A. 2007, *MNRAS*, 379, 1155
- Chiappini, C., Matteucci, F., & Gratton, R. 1997, *ApJ*, 477, 765
- Chiba, R., & Schönrich, R. 2021, *MNRAS*, 505, 2412
- Chiba, R., Friske, J. K. S., & Schönrich, R. 2021, *MNRAS*, 500, 4710
- Clarke, J. P., Wegg, C., Gerhard, O., et al. 2019, *MNRAS*, 489, 3519
- Cohen, R. S., Dame, T. M., & Thaddeus, P. 1986, *ApJS*, 60, 695
- Dame, T. M., Elmegreen, B. G., Cohen, R. S., & Thaddeus, P. 1986, *ApJ*, 305, 892
- Debattista, V. P., Ness, M., Gonzalez, O. A., et al. 2017, *MNRAS*, 469, 1587
- Dehnen, W. 1998, *AJ*, 115, 2384
- Dehnen, W. 2000, *AJ*, 119, 800
- De Silva, G. M., Freeman, K. C., Bland-Hawthorn, J., Asplund, M., & Bessell, M. S. 2007, *AJ*, 133, 694
- Di Matteo, P., Fragkoudi, F., Khoperskov, S., et al. 2019a, *A&A*, 628, A11
- Di Matteo, P., Haywood, M., Lehnert, M. D., et al. 2019b, *A&A*, 632, A4
- Dobbs, C. L., Theis, C., Pringle, J. E., & Bate, M. R. 2010, *MNRAS*, 403, 625
- D’Onghia, E., & Aguerri, J. A. 2020, *ApJ*, 890, 117
- Eggen, O. J. 1965, *Moving Groups of Stars*, 111
- Eilers, A.-C., Hogg, D. W., Rix, H.-W., & Ness, M. K. 2019, *ApJ*, 871, 120
- Famaey, B., Siebert, A., & Jorissen, A. 2008, *A&A*, 483, 453
- Faure, C., Siebert, A., & Famaey, B. 2014, *MNRAS*, 440, 2564
- Fragkoudi, F., Katz, D., Trick, W., et al. 2019, *MNRAS*, 488, 3324
- Fragkoudi, F., Grand, R. J. J., Pakmor, R., et al. 2020, *MNRAS*, 494, 5936
- Frisk, J. K. S., & Schönrich, R. 2019, *MNRAS*, 490, 5414
- Fujii, M. S., Bédorf, J., Baba, J., & Portegies Zwart, S. 2019, *MNRAS*, 482, 1983
- Fukushige, T., Makino, J., & Kawai, A. 2005, *PASJ*, 57, 1009
- Fux, R. 2001, *A&A*, 373, 511
- Gaia Collaboration (Katz, D., et al.) 2018a, *A&A*, 616, A11
- Gaia Collaboration (Brown, A. G. A., et al.) 2018b, *A&A*, 616, A1
- Gaia Collaboration (Brown, A. G. A., et al.) 2021a, *A&A*, 649, A1
- Gaia Collaboration (Antoja, T., et al.) 2021b, *A&A*, 649, A8
- Georgelin, Y. M., & Georgelin, Y. P. 1976, *A&A*, 49, 57
- Gerin, M., Combes, F., & Athanassoula, E. 1990, *A&A*, 230, 37
- Gómez, F. A., Minchev, I., Villalobos, Á., O’Shea, B. W., & Williams, M. E. K. 2012, *MNRAS*, 419, 2163
- Gómez, F. A., Minchev, I., O’Shea, B. W., et al. 2013, *MNRAS*, 429, 159
- Grabelsky, D. A., Cohen, R. S., Bronfman, L., & Thaddeus, P. 1988, *ApJ*, 331, 181
- Grand, R. J. J., Bovy, J., Kawata, D., et al. 2015, *MNRAS*, 453, 1867
- Grand, R. J. J., Springel, V., Kawata, D., et al. 2016, *MNRAS*, 460, L94
- GRAVITY Collaboration (Abuter, R., et al.) 2018, *A&A*, 615, L15
- Halle, A., Di Matteo, P., Haywood, M., & Combes, F. 2015, *A&A*, 578, A58
- Hayden, M. R., Bland-Hawthorn, J., Sharma, S., et al. 2020, *MNRAS*, 493, 2952
- Haywood, M., Di Matteo, P., Lehnert, M. D., Katz, D., & Gómez, A. 2013, *A&A*, 560, A109

- Haywood, M., Snaith, O., Lehnert, M. D., Di Matteo, P., & Khoperskov, S. 2019, *A&A*, **625**, A105
- Helmi, A., Navarro, J. F., Nordström, B., et al. 2006, *MNRAS*, **365**, 1309
- Helmi, A., Williams, M., Freeman, K. C., Bland-Hawthorn, J., & De Silva, G. 2014, *ApJ*, **791**, 135
- Hottier, C., Babusiaux, C., & Arenou, F. 2020, *A&A*, **641**, A79
- Hou, L. G., & Han, J. L. 2014, *A&A*, **569**, A125
- Hou, L. G., Han, J. L., & Shi, W. B. 2009, *A&A*, **499**, 473
- Hunt, J. A. S., Hong, J., Bovy, J., Kawata, D., & Grand, R. J. J. 2018, *MNRAS*, **481**, 3794
- Hunt, J. A. S., Bub, M. W., Bovy, J., et al. 2019, *MNRAS*, **490**, 1026
- Hunt, J. A. S., Johnston, K. V., Pettitt, A. R., et al. 2020, *MNRAS*, **497**, 818
- Hunter, J. D. 2007, *Comput. Sci. Eng.*, **9**, 90
- Jean-Baptiste, I., Di Matteo, P., Haywood, M., et al. 2017, *A&A*, **604**, A106
- Kamdar, H., Conroy, C., Ting, Y.-S., et al. 2019, *ApJ*, **884**, 173
- Katz, D., Gomez, A., Haywood, M., Snaith, O., & Di Matteo, P. 2021, *A&A*, **655**, A111
- Kawata, D., Baba, J., Ciucă, I., et al. 2018, *MNRAS*, **479**, L108
- Khanna, S., Sharma, S., Tepper-Garcia, T., et al. 2019, *MNRAS*, **489**, 4962
- Khoperskov, S., Mastrobuono-Battisti, A., Di Matteo, P., & Haywood, M. 2018a, *A&A*, **620**, A154
- Khoperskov, S., Di Matteo, P., Haywood, M., & Combes, F. 2018b, *A&A*, **611**, L2
- Khoperskov, S., Di Matteo, P., Gerhard, O., et al. 2019, *A&A*, **622**, L6
- Khoperskov, S., Gerhard, O., Di Matteo, P., et al. 2020a, *A&A*, **634**, L8
- Khoperskov, S., Di Matteo, P., Haywood, M., Gómez, A., & Snaith, O. N. 2020b, *A&A*, **638**, A144
- Kushniruk, I., & Bensby, T. 2019, *A&A*, **631**, A47
- Kushniruk, I., Schirmer, T., & Bensby, T. 2017, *A&A*, **608**, A73
- Kushniruk, I., Bensby, T., Feltzing, S., et al. 2020, *A&A*, **638**, A154
- Lallement, R., Babusiaux, C., Vergely, J. L., et al. 2019, *A&A*, **625**, A135
- Laporte, C. F. P., Minchev, I., Johnston, K. V., & Gómez, F. A. 2019, *MNRAS*, **485**, 3134
- Lee, Y. S., Beers, T. C., An, D., et al. 2011, *ApJ*, **738**, 187
- Leung, H. W., & Bovy, J. 2019, *MNRAS*, **483**, 3255
- Liang, X., Zhao, J., Chen, Y., et al. 2019, *ApJ*, **887**, 193
- Lindegren, L., Bastian, U., Biermann, M., et al. 2021a, *A&A*, **649**, A4
- Lindegren, L., Klioner, S. A., Hernández, J., et al. 2021b, *A&A*, **649**, A2
- Luo, A. L., Zhao, Y.-H., Zhao, G., et al. 2015, *Res. Astron. Astrophys.*, **15**, 1095
- Mackereth, J. T., Schiavon, R. P., Pfeffer, J., et al. 2019, *MNRAS*, **482**, 3426
- Majewski, S. R., Schiavon, R. P., Frinchaboy, P. M., et al. 2017, *AJ*, **154**, 94
- Marshall, D. J., Robin, A. C., Reylic, C., Schultheis, M., & Picaud, S. 2006, *A&A*, **453**, 635
- Martinez-Medina, L., Pichardo, B., Peimbert, A., & Valenzuela, O. 2019, *MNRAS*, **485**, L104
- Mayer, L., & Wadsley, J. 2004, *MNRAS*, **347**, 277
- McKinney, W. 2010, in *Proceedings of the 9th Python in Science Conference*, eds. S. van der Walt, & J. Millman, 56
- Michtchenko, T. A., Lépine, J. R. D., Barros, D. A., & Vieira, R. S. S. 2018, *A&A*, **615**, A10
- Minchev, I., Quillen, A. C., Williams, M., et al. 2009, *MNRAS*, **396**, L56
- Miyamoto, M., & Nagai, R. 1975, *PASJ*, **27**, 533
- Monari, G., Famaey, B., & Siebert, A. 2016a, *MNRAS*, **457**, 2569
- Monari, G., Famaey, B., Siebert, A., et al. 2016b, *MNRAS*, **461**, 3835
- Monari, G., Kawata, D., Hunt, J. A. S., & Famaey, B. 2017, *MNRAS*, **466**, L113
- Monari, G., Famaey, B., Minchev, I., et al. 2018, *Res. Notes Am. Astron. Soc.*, **2**, 32
- Monari, G., Famaey, B., Siebert, A., et al. 2019a, *A&A*, **632**, A107
- Monari, G., Famaey, B., Siebert, A., Wegg, C., & Gerhard, O. 2019b, *A&A*, **626**, A41
- Mróz, P., Udalski, A., Skowron, D. M., et al. 2019, *ApJ*, **870**, L10
- Navarro, J. F., Helmi, A., & Freeman, K. C. 2004, *ApJ*, **601**, L43
- Nissen, P. E., & Schuster, W. J. 2010, *A&A*, **511**, L10
- Nordström, B., Mayor, M., Andersen, J., et al. 2004, *A&A*, **418**, 989
- Perez, F., & Granger, B. E. 2007, *Comput. Sci. Eng.*, **9**, 21
- Pérez-Villegas, A., Portail, M., & Gerhard, O. 2017a, *MNRAS*, **464**, L80
- Pérez-Villegas, A., Portail, M., Wegg, C., & Gerhard, O. 2017b, *ApJ*, **840**, L2
- Pettitt, A. R., & Wadsley, J. W. 2018, *MNRAS*, **474**, 5645
- Piskunov, N., & Valentí, J. A. 2017, *A&A*, **597**, A16
- Plummer, H. C. 1911, *MNRAS*, **71**, 460
- Poggio, E., Drimmel, R., Cantat-Gaudin, T., et al. 2021, *A&A*, **651**, A104
- Portail, M., Gerhard, O., Wegg, C., & Ness, M. 2017, *MNRAS*, **465**, 1621
- Purcell, C. W., Bullock, J. S., Tollerud, E. J., Rocha, M., & Chakrabarti, S. 2011, *Nature*, **477**, 301
- Quillen, A. C., & Minchev, I. 2005, *AJ*, **130**, 576
- Quillen, A. C., Dougherty, J., Bagley, M. B., Minchev, I., & Comparetta, J. 2011, *MNRAS*, **417**, 762
- Quillen, A. C., Carrillo, I., Anders, F., et al. 2018, *MNRAS*, **480**, 3132
- Quinn, P. J., & Goodman, J. 1986, *ApJ*, **309**, 472
- Ramírez, I., & Allende Prieto, C. 2011, *ApJ*, **743**, 135
- Ramos, P., Antoja, T., & Figueras, F. 2018, *A&A*, **619**, A72
- Ramya, P., Reddy, B. E., & Lambert, D. L. 2012, *MNRAS*, **425**, 3188
- Reid, M. J., Menten, K. M., Brunthaler, A., et al. 2014, *ApJ*, **783**, 130
- Reid, M. J., Menten, K. M., Brunthaler, A., et al. 2019, *ApJ*, **885**, 131
- Russeil, D. 2003, *A&A*, **397**, 133
- Saburova, A. S., Katkov, I. Y., Khoperskov, S. A., Zasov, A. V., & Uklein, R. I. 2017, *MNRAS*, **470**, 20
- Sanders, J. L., Smith, L., & Evans, N. W. 2019, *MNRAS*, **488**, 4552
- Schönrich, R., & Dehnen, W. 2018, *MNRAS*, **478**, 3809
- Schönrich, R., Binney, J., & Dehnen, W. 2010, *MNRAS*, **403**, 1829
- Sellwood, J. A., & Binney, J. J. 2002, *MNRAS*, **336**, 785
- Sellwood, J. A., Trick, W. H., Carlberg, R. G., Coronado, J., & Rix, H.-W. 2019, *MNRAS*, **484**, 3154
- Siebert, A., Famaey, B., Minchev, I., et al. 2011, *MNRAS*, **412**, 2026
- Siebert, A., Famaey, B., Binney, J., et al. 2012, *MNRAS*, **425**, 2335
- Skuljan, J., Cottrell, P. L., Hearnshaw, J. B., et al. 1997, in *Hipparcos - Venice '97*, eds. R. M. Bonnet, E. Høg, P. L. Bernacca et al., *ESA Spec. Publ.*, **402**, 525
- Spitoni, E., Cescutti, G., Minchev, I., et al. 2019, *A&A*, **628**, A38
- Taylor, J. H., & Cordes, J. M. 1993, *ApJ*, **411**, 674
- Taylor, M. B. 2005, in *TOPCAT & STIL: Starlink Table/VOTable Processing Software*, eds. P. Shopbell, M. Britton, & R. Ebert, *ASP Conf. Ser.*, **347**, 29
- Ting, Y.-S., Conroy, C., Rix, H.-W., & Cargile, P. 2019, *ApJ*, **879**, 69
- Trick, W. H. 2022, *MNRAS*, **509**, 844
- van der Walt, S., Colbert, S. C., & Varoquaux, G. 2011, *Comput. Sci. Eng.*, **13**, 22
- Vasiliev, E. 2019, *MNRAS*, **482**, 1525
- Virtanen, P., Gommers, R., Oliphant, T. E., et al. 2020, *Nat. Methods*, **17**, 261
- Wang, H. F., López-Corredoira, M., Huang, Y., et al. 2020a, *MNRAS*, **491**, 2104
- Wang, H. F., Huang, Y., Zhang, H. W., et al. 2020b, *ApJ*, **902**, 70
- Wegg, C., Gerhard, O., & Portail, M. 2015, *MNRAS*, **450**, 4050
- Wegg, C., Rojas-Arriagada, A., Schultheis, M., & Gerhard, O. 2019, *A&A*, **632**, A121
- Wheeler, A., Ness, M., Buder, S., et al. 2020, *ApJ*, **898**, 58
- Wheeler, A., Abril-Cabezas, I., Trick, W. H., Fragkoudi, F., & Ness, M. 2021, *ApJ*, submitted [arXiv:2105.05263]
- Widrow, L. M., Gardner, S., Yanny, B., Dodelson, S., & Chen, H.-Y. 2012, *ApJ*, **750**, L41
- Widrow, L. M., Barber, J., Chequers, M. H., & Cheng, E. 2014, *MNRAS*, **440**, 1971
- Williams, M. E. K., Freeman, K. C., Helmi, A., & RAVE Collaboration 2009, in *The Galaxy Disk in Cosmological Context*, eds. J. Andersen, B. Nordström, & J. Bland-Hawthorn, *IAU Symp.*, **254**, 139
- Williams, M. E. K., Steinmetz, M., Binney, J., et al. 2013, *MNRAS*, **436**, 101
- Wozniak, H. 2020, *ApJ*, **889**, 81
- Xiang, M. S., Liu, X. W., Yuan, H. B., et al. 2017, *MNRAS*, **467**, 1890
- Xiang, M., Ting, Y.-S., Rix, H.-W., et al. 2019, *ApJS*, **245**, 34
- Zhao, J. K., Zhao, G., Chen, Y. Q., et al. 2014, *ApJ*, **787**, 31

## Appendix A: Linking chemical abundances with $R - R_g$ value

In Fig. A.1 we present the well-known  $[\alpha/\text{Fe}] - [\text{Fe}/\text{H}]$  plane together with  $[\alpha/\text{Fe}] - |R - R_g|$  and  $|R - R_g| - [\text{Fe}/\text{H}]$  relations for G3RV2+G.A.L. subsamples providing an important chemo-kinematical information about stellar populations in the MW. The  $[\alpha/\text{Fe}] - [\text{Fe}/\text{H}]$  relation for all adopted surveys shows the well-known dichotomy that implies the presence of two main populations, usually associated with thick (high- $\alpha$ ) and thin (low- $\alpha$ ) components (see e.g. [Bensby et al. 2014](#); [Haywood et al. 2013](#)). The kinematical diversity of stellar populations of these components is clearly visible when we colour-code the  $[\alpha/\text{Fe}] - [\text{Fe}/\text{H}]$  relation by the mean  $R - R_g$  value (Fig. A.1a, e, i), where the thin disk (low- $\alpha$ ) mostly contains cold stars with a low radial oscillation amplitude that gradually increases towards high- $\alpha$  sequence. A third distinct component is also visible at low metallicities ( $[\text{Fe}/\text{H}] < -0.5$ ), where  $R - R_g \gtrsim 5$  kpc corresponds to the accreted stars ([Nissen & Schuster 2010](#)), which we also find as a separate component in  $R - R_g$  distributions (see Fig. 6). Interestingly, the  $[\alpha/\text{Fe}] - [\text{Fe}/\text{H}]$  relation colour-coded by the mean  $R - R_g$  looks very similar to the relation presented by [Mackereth et al. \(2019\)](#), [Hayden et al. \(2020\)](#) for the Snd stars colour-coded by the orbital eccentricity. These three main components are also revealed in the  $[\alpha/\text{Fe}] - |R - R_g|$  relation. The decrease in stellar radial oscillations with  $[\text{Fe}/\text{H}]$  is clearly visible in panels c, g, and k. Another feature is the very hot stars with  $R - R_g > 5$  kpc up to solar metallicities. The understanding of this population may provide some new constraints on the parameters of the last MW merger and the follow-up disk heating. Because the low- $\alpha$  stars mainly contain stars with low  $R - R_g$  values (see panels d, h, and l), our results presented in Fig. 7 suggest that the MW spiral arms show a larger fraction of thin-disk stars.

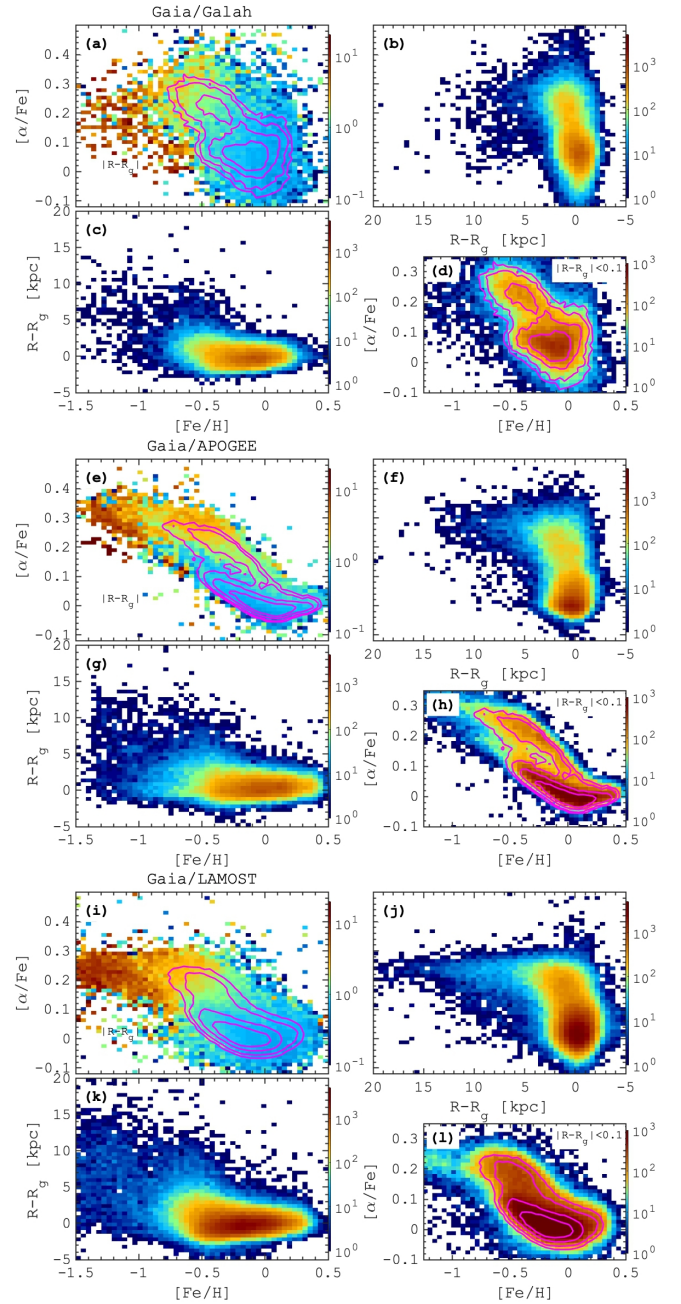


**Fig. A.1.** Relation between chemical abundances as a function of  $R - R_g$  for Galah (a-d), APOGEE (e-h), and LAMOST (i-l) cross-matched with Gaia DR2 (G3RV2). Panels a, e, and i show the  $[\alpha/\text{Fe}] - [\text{Fe}/\text{H}]$  relation colour-coded by the mean  $|R - R_g|$  value in log scale. Panels b, f, and j show the number of stars in  $[\alpha/\text{Fe}] - |R - R_g|$  plane. Panels c, g, and k show the number of stars in  $|R - R_g| - [\text{Fe}/\text{H}]$  plane. Finally, panels d, h, and l show the number of stars with  $|R - R_g| < 0.25$  in  $[\alpha/\text{Fe}] - [\text{Fe}/\text{H}]$  plane. Magenta contours in the  $[\alpha/\text{Fe}] - [\text{Fe}/\text{H}]$  planes show the distribution of the total number of stars.